Available online at www.sciencedirect.com
ScienceDirect
Comput. Methods Appl. Mech. Engrg. 376 (2021) 113589
Computer methods in applied mechanics and engineering
www.elsevier.com/locate/cma

A new efficient fully-decoupled and second-order time-accurate scheme for Cahn–Hilliard phase-field model of three-phase incompressible flow

Xiaofeng Yang

Department of Mathematics, University of South Carolina, Columbia, SC 29208, USA

Received 9 July 2020; received in revised form 13 November 2020; accepted 14 November 2020
Available online 8 January 2021

Abstract

For the highly coupled and nonlinear Cahn–Hilliard phase-field model of three-phase incompressible flow, how to establish a fully-decoupled numerical scheme with second-order time accuracy has always been a very difficult and unsolved problem. In this paper, we propose a novel decoupling method, which only needs to solve several decoupling linear elliptic equations with constant coefficients at each time step to obtain a numerical solution with second-order time accuracy. The key idea is to introduce two nonlocal auxiliary variables into the system, one of which is used to linearize the nonlinear potential, and the other is used to introduce an ordinary differential equation to deal with the nonlinear coupling terms with "*zero-energy-contribution*" characteristics. We strictly prove the solvability and unconditional energy stability of the scheme, and conduct numerical simulations in 2D and 3D to show the accuracy and stability of the scheme numerically. To the best of the author's knowledge, the method developed in this paper is the first second-order fully-decoupled scheme for the hydrodynamics coupled phase-field model.

Keywords: Fully-decoupled; Second-order; Phase-field; Cahn–Hilliard; Three-phase; Unconditional energy stability

1. Introduction

Unlike the phase-field model of the two-phase flow system that requires only one phase-field variable to represent the volume fraction of two phases, the Cahn–Hilliard phase-field model of three-phase incompressible flows usually requires three phase-field variables to formally represent the volume (or mass) of each component [1–4]. In the total free energy, the hydrophilic–hydrophobic tendency of each phase-field variable is independent, but to ensure the so-called free-leakage condition of the system, a Lagrange multiplier needs to be added in each Cahn–Hilliard equation, thereby establishing a highly nonlinear and coupled system. Not only that, for some specific physical phenomena, such as the so-called "total spreading" situation, but it is also necessary to add some coupled higher-order terms to the total free energy to ensure the well-posedness of the entire system. Finally, after combining the Navier–Stokes equation describing the characteristics of the incompressible flow field, a highly coupled and nonlinear complex dynamical system is obtained. Among them, the coupling terms can be divided into two categories, one is formulated

E-mail address: xfyang@math.sc.edu.

https://doi.org/10.1016/j.cma.2020.113589
0045-7825/

from the energy variation, the other comes from fluid properties, including the advection and surface tension from the three fluid components.

We recall that for this complex model, there are still some successful attempts to develop numerical algorithms that can achieve unconditional energy stability, or fully-decoupling structure, or both. Some are for the partial model without the flow field, such as the nonlinear method in [3,4], Invariant Energy Quadratization (IEQ) method in [5], Scalar Auxiliary Variable (SAV) method in [6,7], etc. For the full model with the flow field, to the best of the author's knowledge, the only fully-decoupled scheme with unconditional energy stability is developed in [8], however, the scheme is only first-order in time, and its computational cost is relatively expensive due to the nonlinear nature. Hence, a natural question arises, why it is so difficult to establish a fully-decoupled and second-order time-accurate scheme, since we all know that there are so many second-order energy-stable numerical schemes for the phase-field models (for example, the linear stabilization [9–12], convex splitting [13–17], IEQ [5,18–22], SAV [18,23–27], nonlinear derivative [28], nonlinear quadrature [29–31] methods, etc.), and the Navier–Stokes equations (for example, the projection-type methods including pressure-correction, velocity-correction, Gauge-method, etc., see [32–35]). Therefore, based on the above facts, it can be considered that simply combining these methods can easily obtain the ideal scheme, that is, a completely decoupled and second-order time-accurate scheme.

However, unfortunately, the current situation is that we still lack sufficient skills to achieve such a scheme, *where the main difficulty lies in how to discretize the advection and surface tension terms.* At present, for these two kinds of terms, the most popular method is to discretize them by using the explicit and implicit combination method or completely implicit method, which will inevitably lead to expensive nonlinear fully-coupled schemes or relatively fast linear fully-coupled schemes, cf. [8,12,17,36–43]. Besides, a decoupling method was developed in [8], the main idea of which is to add a stabilization term to the explicit advection velocity term, thereby decoupling the momentum equation and the Cahn–Hilliard equation ingeniously. However, the disadvantage is that the added stabilization term contains an implicitly processed chemical potential, which leads to the need to solve the Cahn–Hilliard equation with variable coefficients at each time step, resulting in a higher computational cost than with constant coefficients. Moreover, the scheme in [8] is only first-order time-accurate, and it seems to be difficult to generalize the idea of stabilization to the second-order version.

Therefore, for the highly challenging three-phase flow-coupled model, this paper attempts to develop an effective scheme from a novel perspective. We expect the scheme is not only unconditionally energy stable, linear, second-order time accurate but also fully-decoupled. We also expect that only a few independent elliptic equations need to be solved at each time step, thereby reducing the actual calculation cost. To this end, on the one hand, we combine some effective methods, such as the projection method for solving the coupling of pressure and velocity, and the SAV method that converts the nonlinear energy potential to the quadratic form of the auxiliary variable, thus a linear scheme is obtained. On the other hand, we develop a novel decoupling method which makes full use of the so-called *"zero-energy-contribution"* characteristics that are satisfied by the advection and surface tension, that is, when deriving the energy law, these two types of terms, after performing the inner product with certain specific functions, will cancel each other without entering the law of energy. Using this feature, we introduce a nonlocal auxiliary variable and design an ordinary differential equation containing the inner product of these terms and specific functions. This equation is trivial at the PDE level because through integrating by parts or using divergence-free condition, all terms contained in the equation can be canceled or equal to zero. However, after discretization, this ODE can help to eliminate all the troublesome nonlinear terms that are explicitly handled, thereby obtaining unconditional energy stability. Moreover, the introduction of this auxiliary variable can decompose each discrete equation into multiple sub-equations, which can be solved independently to achieve the fully-decoupling structure.

Combining all these numerical techniques, we propose a novel scheme that only requires solving several linear and fully-decoupled elliptic equations with constant coefficients at each time step. We also give the rigorous proofs of the unconditional energy stability and further simulate various numerical examples in 2D and 3D to demonstrate stability and accuracy. It is worth noting that as long as the coupling term satisfies the "*zero-energy-contribution*" characteristic, the decoupling technique proposed in this paper can be universally applied to achieve fully-decoupling type schemes. To the author's knowledge, the method developed in this paper is not only the first second-order fully-decoupled scheme for the particular three-phase model, but also the first method to generate the fully-decoupled scheme for coupled models with "*zero-energy-contribution*" terms.

The rest of the paper is organized as follows. In Section 2, we briefly describe the Cahn–Hilliard phase-field model of three-phase incompressible flow and derive its associated PDE energy dissipation law. In Section 3, we

introduce the numerical scheme, explain its implementations in detail, and prove its solvability and discrete energy dissipation law rigorously. In Section 4, many numerical examples are given to illustrate the accuracy and efficiency of the scheme. We finally give some concluding remarks in Section 5.

2. Model system

We briefly outline the Cahn–Hilliard phase-field system, which simulates the three immiscible fluid components proposed in [2–4]. A domain Ω is an open bounded, connected, subset in $\mathbb{R}^d$ of $d = 2, 3$, with a sufficiently smooth boundary. We assume ϕ_i $(i = 1, 2, 3)$ to be the ith phase-field variable which represents the volume of the ith component in the fluid mixture, such that

$$\phi_i(\boldsymbol{x}, t) = \begin{cases} 1 & \text{inside the } i\text{th component,} \\ 0 & \text{outside the } i\text{th component,} \end{cases} \tag{2.1}$$

where $\boldsymbol{x} \in \Omega$, t is time in $[0, T]$. A smooth layer with the thickness ϵ is used to connect the interface between 0 and 1. Assuming the mixture being perfect (called as free-leakage condition), the three unknowns ϕ_1, ϕ_2, ϕ_3 are linked by the following relationship:

$$\phi_1(\boldsymbol{x}, t) + \phi_2(\boldsymbol{x}, t) + \phi_3(\boldsymbol{x}, t) = 1. \tag{2.2}$$

There are several ways to promote the two-phase model to the three-phase case, cf. [1–4]. In this article, we use the model developed in [2–4] and assume the total free energy as

$$E(\phi_1, \phi_2, \phi_3) = \int_\Omega \Big(\frac{3\epsilon}{8} L(\phi_1, \phi_2, \phi_3) + \frac{12}{\epsilon} F(\phi_1, \phi_2, \phi_3) \Big) d\boldsymbol{x}, \tag{2.3}$$

where ϵ is the order parameter to characterize the interfacial width, $L(\phi_1, \phi_2, \phi_3)$ is the linear part, and $F(\phi_1, \phi_2, \phi_3)$ is the nonlinear part.

The linear part is given as

$$L(\phi_1, \phi_2, \phi_3) = \Sigma_1 |\nabla \phi_1|^2 + \Sigma_2 |\nabla \phi_2|^2 + \Sigma_3 |\nabla \phi_3|^2, \tag{2.4}$$

where the coefficient Σ_i represents the "spreading" coefficient of the ith at the interface between jth phase and kth phase. One can deduce that the following conditions hold between the three surface tension parameters σ_{ij} $(\sigma_{12}, \sigma_{13}, \sigma_{23})$ and three spreading coefficients $(\Sigma_1, \Sigma_2, \Sigma_3)$ (see [2–4]):

$$\Sigma_i = \sigma_{ij} + \sigma_{ik} - \sigma_{jk}, i = 1, 2, 3. \tag{2.5}$$

Note Σ_i might not be always positive. If $\Sigma_i > 0$, it means that the spreading is "partial", if $\Sigma_i < 0$, it is called "total".

The nonlinear potential $F(\phi_1, \phi_2, \phi_3)$ is given as:

$$\begin{aligned} F(\phi_1, \phi_2, \phi_3) =& \sigma_{12}\phi_1^2\phi_2^2 + \sigma_{13}\phi_1^2\phi_3^2 + \sigma_{23}\phi_2^2\phi_3^2 \\ &+ \phi_1\phi_2\phi_3(\Sigma_1\phi_1 + \Sigma_2\phi_2 + \Sigma_3\phi_3) + 3\Lambda\phi_1^2\phi_2^2\phi_3^2, \end{aligned} \tag{2.6}$$

where Λ is a non-negative constant. Since ϕ_1, ϕ_2, ϕ_3 satisfy the free-leakage condition (2.2), $F(\phi_1, \phi_2, \phi_3)$ can be rewritten as

$$F(\phi_1, \phi_2, \phi_3) = F_0(\phi_1, \phi_2, \phi_3) + P(\phi_1, \phi_2, \phi_3), \tag{2.7}$$

where

$$\begin{cases} F_0(\phi_1, \phi_2, \phi_3) = \dfrac{\Sigma_1}{2}\phi_1^2(1-\phi_1)^2 + \dfrac{\Sigma_2}{2}\phi_2^2(1-\phi_2)^2 + \dfrac{\Sigma_3}{2}\phi_3^2(1-\phi_3)^2, \\ P(\phi_1, \phi_2, \phi_3) = 3\Lambda\phi_1^2\phi_2^2\phi_3^2. \end{cases} \tag{2.8}$$

Regarding the total free energy and surface tension coefficients, some remarks are given as follows (see the details in [4]):

Remark 2.1. Let σ_{12}, σ_{13} and σ_{23} be three positive numbers and Σ_1, Σ_2 and Σ_3 defined by (2.5). For any $\Lambda > 0$, the bulk free energy $F(\phi_1, \phi_2, \phi_3)$ defined in (2.7) is bounded from below if ϕ_1, ϕ_2, ϕ_3 satisfies the free-leakage condition (2.2).

Remark 2.2. For any $\xi_1+\xi_2+\xi_3=0$, there exists a constant $\underline{\Sigma}>0$ such that

$$\Sigma_1|\xi_1|^2+\Sigma_2|\xi_2|^2+\Sigma_3|\xi_3|^2\geq \underline{\Sigma}\Big(|\xi_1|^2+|\xi_2|^2+|\xi_3|^2\Big)\geq 0, \tag{2.9}$$

if and only if the following conditions are valid:

$$\Sigma_1\Sigma_2+\Sigma_1\Sigma_3+\Sigma_2\Sigma_3>0,\ \Sigma_i+\Sigma_j>0, \forall i\neq j. \tag{2.10}$$

Furthermore, the lower bound only depends on Σ_1, Σ_2, Σ_3 and Λ. Hence, if ϕ_1,ϕ_2,ϕ_3 satisfies the free-leakage condition (2.2), we derive $\nabla\phi_1+\nabla\phi_2+\nabla\phi_3=0$. Hence, from (2.9), we get

$$\sum_{i=1}^{3}\Sigma_i\|\nabla\phi_i\|^2\geq\underline{\Sigma}\sum_{i=1}^{3}\|\nabla\phi_i\|^2\geq 0. \tag{2.11}$$

Remark 2.3. To form a meaningful physical system, the energy potential $F(\phi_1,\phi_2,\phi_3)$ defined in (2.7) must be bounded from below. For partial spreading case ($\Sigma_i>0$, $\forall i$), one can assume that $\Lambda=0$ since $F_0(\phi_1,\phi_2,\phi_3)\geq 0$ is naturally fulfilled. For the total spreading case, Λ has to be non-zero. Moreover, in order to ensure the non-negativity of F, Λ must be large enough.

For the 3D case, it is shown in [4] that when $P(\phi_1,\phi_2,\phi_3)$ takes the following form, the bulk energy F is bounded from below:

$$P(\phi_1,\phi_2,\phi_3)=3\Lambda\phi_1^2\phi_2^2\phi_3^2(\phi_\alpha(\phi_1)+\phi_\alpha(\phi_2)+\phi_\alpha(\phi_3)) \tag{2.12}$$

where $\phi_\alpha(x)=\frac{1}{(1+x^2)^\alpha}$ with $0<\alpha\leq\frac{8}{17}$.

Since (2.8) is more commonly used in [2,4], we also adopt it for simplicity. It is clear that the numerical scheme developed in this paper can handle (2.9) or (2.12) without any essential difficulties.

To couple the fluid momentum into the system, the total free energy becomes

$$E_{tot}(\mathbf{u},\phi_1,\phi_2,\phi_3)=\int_\Omega\Big(\frac{1}{2}|\mathbf{u}|^2+\frac{3\epsilon}{8}L(\phi_1,\phi_2,\phi_3)+\frac{12}{\epsilon}F(\phi_1,\phi_2,\phi_3)\Big)d\boldsymbol{x}, \tag{2.13}$$

where $\mathbf{u}$ represents the fluid velocity.

Assuming that the fluid is incompressible and follows the generalized Fick's law, that is, the mass flux is proportional to the gradient of the chemical potential, we can derive the following three-phase Cahn–Hilliard model coupled with hydrodynamics:

$$\phi_{it}+\nabla\cdot(\mathbf{u}\phi_i)=M\Delta\frac{\mu_i}{\Sigma_i}, \tag{2.14}$$

$$\mu_i=-\frac{3}{4}\epsilon\Sigma_i\Delta\phi_i+\frac{12}{\epsilon}(f_i+\beta_L),\ i=1,2,3, \tag{2.15}$$

$$\mathbf{u}_t+\mathbf{u}\cdot\nabla\mathbf{u}-\nu\Delta\mathbf{u}+\nabla p+\sum_{i=1}^{3}\phi_i\nabla\mu_i=0, \tag{2.16}$$

$$\nabla\cdot\mathbf{u}=0, \tag{2.17}$$

where M is the mobility parameter, $f_i=\partial_i F$, p is the pressure, ν is the fluid viscosity, β_L is the Lagrange multiplier to ensure the free-leakage condition (2.2) and it can be derived as

$$\beta_L=-\Sigma_T\Big(\frac{f_1}{\Sigma_1}+\frac{f_2}{\Sigma_2}+\frac{f_3}{\Sigma_3}\Big)\ \text{with}\ \frac{1}{\Sigma_T}=\frac{1}{\Sigma_1}+\frac{1}{\Sigma_2}+\frac{1}{\Sigma_3}. \tag{2.18}$$

The boundary conditions of the system are one of the following two types:

$$\text{(i) all variables are periodic, or (ii) } \mathbf{u}|_{\partial\Omega}=\partial_{\mathbf{n}}\phi_i|_{\partial\Omega}=\partial_{\mathbf{n}}\mu_i|_{\partial\Omega}=0,\ i=1,2,3, \tag{2.19}$$

where $\mathbf{n}$ is the unit outward normal to the boundary $\partial\Omega$. The initial conditions are given by

$$\mathbf{u}|_{(t=0)}=\mathbf{u}^0,\ p|_{(t=0)}=p^0,\ \phi_i|_{(t=0)}=\phi_i^0, \tag{2.20}$$

where the initial condition also satisfies the free-leakage condition $\phi_1^0+\phi_2^0+\phi_3^0=1$.

Remark 2.4. It can be proved that the three-phase system (2.14)–(2.15) is equivalent to the following PDE system using two variables

$$\begin{cases} \phi_{it} + \nabla \cdot (\mathbf{u}\phi_i) = M\Delta \dfrac{\mu_i}{\Sigma_i}, \\ \mu_i = -\dfrac{3}{4}\epsilon \Sigma_i \Delta \phi_i + \dfrac{12}{\epsilon}(f_i + \beta_L),\ i = 1, 2, \end{cases} \tag{2.21}$$

where ϕ_3 and μ_3 are given by the following explicit formula:

$$\phi_1 + \phi_2 + \phi_3 = 1, \tag{2.22}$$

$$\frac{\mu_1}{\Sigma_1} + \frac{\mu_2}{\Sigma_2} + \frac{\mu_3}{\Sigma_3} = 0. \tag{2.23}$$

Since the proof is quite similar to Theorem 3.1, we omit the details here.

The model equations (2.14)–(2.17) follow a dissipative energy law. By taking the L^2 inner product of (2.14) with μ_i, of (2.15) with $-\phi_{it}$, of (2.16) with $\mathbf{u}$, and performing integration by parts, we can obtain

$$(\phi_{it}, \mu_i) = -M\Sigma_i \left\| \frac{\nabla \mu_i}{\Sigma_i} \right\|^2 - \int_\Omega \nabla \cdot (\mathbf{u}\phi_i)\mu_i d\boldsymbol{x}, \tag{2.24}$$

$$-(\mu_i, \phi_{it}) + \frac{3}{8}\epsilon \Sigma_i d_t \|\nabla \phi_i\|^2 + \frac{12}{\epsilon} d_t \int_\Omega F(\phi_i) d\boldsymbol{x} = -\frac{12}{\epsilon}(\beta_L, \phi_{it}), \tag{2.25}$$

$$\frac{1}{2} d_t \|\mathbf{u}\|^2 + \nu \|\nabla \mathbf{u}\|^2 - (p, \nabla \cdot \mathbf{u}) = -\int_\Omega (\mathbf{u} \cdot \nabla)\mathbf{u} \cdot \mathbf{u} d\boldsymbol{x} - \sum_{i=1}^{3} \int_\Omega \phi_i \nabla \mu_i \cdot \mathbf{u} d\boldsymbol{x}. \tag{2.26}$$

Then, we take the summation of (2.24) and (2.25) for $i = 1, 2, 3$, and combine the obtained results with (2.26). Using (2.17) for the pressure term and $(\beta_L, (\phi_1 + \phi_2 + \phi_3)_t) = (\beta_L, (1)_t) = 0$ from (2.22), we obtain the energy dissipative law as

$$\begin{aligned} &\frac{d}{dt} E_{tot}(\mathbf{u}, \phi_1, \phi_2, \phi_3) \\ &\quad = -\nu \|\nabla \mathbf{u}\|^2 - M\left(\Sigma_1 \left\| \frac{\nabla \mu_1}{\Sigma_1} \right\|^2 + \Sigma_2 \left\| \frac{\nabla \mu_2}{\Sigma_2} \right\|^2 + \Sigma_3 \left\| \frac{\nabla \mu_3}{\Sigma_3} \right\|^2 \right) \\ &\quad \le -\nu \|\nabla \mathbf{u}\|^2 - M\underline{\Sigma}\left(\left\| \frac{\nabla \mu_1}{\Sigma_1} \right\|^2 + \left\| \frac{\nabla \mu_2}{\Sigma_2} \right\|^2 + \left\| \frac{\nabla \mu_3}{\Sigma_3} \right\|^2 \right), \end{aligned} \tag{2.27}$$

where the last inequality is derived by using (2.9) since (μ_1, μ_2, μ_3) satisfies the condition (2.23).

Remark 2.5. When deriving the PDE energy law (2.27), due to the divergence-free condition, the advection term vanishes. The advection and surface tension terms are offset by using integration by parts, i.e.,

$$\int_\Omega \left(\phi_i \nabla \mu_i \cdot \mathbf{u} + \nabla \cdot (\mathbf{u}\phi_i)\mu_i \right) d\boldsymbol{x} = 0, i = 1, 2, 3. \tag{2.28}$$

This means that the advection and surface tension terms do not contribute to the total free energy or energy diffusivity, that is, they satisfy the "*zero-energy-contribution*" feature, which provides us with inspiration for designing a fully-decoupled scheme given in the next section.

3. Numerical schemes

The purpose of this section is to construct a fully-decoupled numerical scheme to solve the flow-coupled phase-field system of three components incompressible flow system (2.14)–(2.17). At the same time, considering the efficiency and accuracy of the algorithm in practice, we also expect that the scheme can satisfy linearity, second-order time accuracy, and unconditional energy stability. The detailed process for developing such a scheme is given as follows.

First, we define the auxiliary function $U(\boldsymbol{x}, t)$ as

$$U = \sqrt{\int_\Omega F(\phi_1, \phi_2, \phi_3) d\boldsymbol{x} + B}, \tag{3.1}$$

where B is any constant such that the radicand is always positive (Note $F(\phi_1, \phi_2, \phi_3)$ is always bounded from below from Remark 2.3).

Second, we define another nonlocal type scalar auxiliary variable: $Q(t) \equiv 1$ which is written as the solution of a simple ordinary differential equation, that reads as

$$\begin{cases} Q_t = 0, \\ Q|_{t=0} = 1. \end{cases} \tag{3.2}$$

Then, by combining the two nonlocal variables U and Q, and the trivial evolution Eq. (3.2), the system (2.14)–(2.17) is reformulated to the following form:

$$\phi_{it} + Q\nabla \cdot (\mathbf{u}\phi_i) = M\Delta \frac{\mu_i}{\Sigma_i}, \tag{3.3}$$

$$\mu_i = -\frac{3}{4}\epsilon \Sigma_i \Delta \phi_i + \frac{12}{\epsilon}(H_i + \beta)U, \ i = 1, 2, 3, \tag{3.4}$$

$$U_t = \frac{1}{2}\sum_{i=1}^{3} \int_\Omega H_i \phi_{it} d\boldsymbol{x}, \tag{3.5}$$

$$\mathbf{u}_t + Q\mathbf{u} \cdot \nabla \mathbf{u} - \nu \Delta \mathbf{u} + \nabla p + Q\sum_{i=1}^{3} \phi_i \nabla \mu_i = 0, \tag{3.6}$$

$$Q_t = \sum_{i=1}^{3} \int_\Omega \nabla \cdot (\mathbf{u}\phi_i)\mu_i d\boldsymbol{x} + \sum_{i=1}^{3} \int_\Omega \phi_i \nabla \mu_i \cdot \mathbf{u} d\boldsymbol{x} + \int_\Omega \mathbf{u} \cdot \nabla \mathbf{u} \cdot \mathbf{u} d\boldsymbol{x}, \tag{3.7}$$

$$\nabla \cdot \mathbf{u} = 0, \tag{3.8}$$

where

$$\beta = -\Sigma_T \left(\frac{H_1}{\Sigma_1} + \frac{H_2}{\Sigma_2} + \frac{H_3}{\Sigma_3} \right), \tag{3.9}$$

$$H_i = \frac{f_i}{\sqrt{\int_\Omega F(\phi_1, \phi_2, \phi_3) d\boldsymbol{x} + B}}. \tag{3.10}$$

Note (3.9) can be also written as the following form,

$$\frac{H_1 + \beta}{\Sigma_1} + \frac{H_2 + \beta}{\Sigma_2} + \frac{H_3 + \beta}{\Sigma_3} = 0. \tag{3.11}$$

The variables $(\mathbf{u}, p, \phi_i, \mu_i, U, Q)$ constitutes a closed PDE system. The initial conditions are given as follows,

$$\begin{cases} \mathbf{u}|_{(t=0)} = \mathbf{u}^0, \ p|_{(t=0)} = p^0, \ \phi_i|_{(t=0)} = \phi_i^0, \ i = 1, 2, 3, \\ U|_{(t=0)} = U^0 = \sqrt{\int_\Omega F(\phi_1^0, \phi_2^0, \phi_3^0) d\boldsymbol{x} + B}, \ Q|_{(t=0)} = 1. \end{cases} \tag{3.12}$$

Note that since Eqs. (3.5) and (3.7) are ODEs that change with time, the boundary conditions for U, Q are not needed at all. So the boundary conditions of the system (3.3)–(3.8) are still (2.19).

Remarkably, in the new system (3.3)–(3.8), we multiply each term that satisfies the "*zero-energy-contribution*" characteristic with the nonlocal variable Q. It is easy to find that, after using integration by parts and the divergence-free condition, the combination of all nonlinear integrations in (3.7) is equal to zero, which means $Q \equiv 1$ and thus the new system (3.3)–(3.8) is equivalent to the original PDE system (2.14)–(2.17). Meanwhile, the new system (3.3)–(3.8) also holds the law of energy dissipation that can be obtained through a similar process to obtain (2.27). Since the discrete-level energy stability proof process follows the same principle, we introduce the following detailed process to make it more clear.

We multiply the L^2 inner product of (3.3) with μ_i to get

$$(\phi_{it}, \mu_i) = -M\Sigma_i \left\| \frac{\nabla \mu_i}{\Sigma_i} \right\|^2 \underbrace{- Q \int_\Omega \nabla \cdot (\mathbf{u}\phi_i)\mu_i d\boldsymbol{x}}_{\mathrm{I}_1}. \tag{3.13}$$

We multiply the L^2 inner product of (3.4) with $-\phi_{it}$ to get

$$-(\mu_i,\phi_{it})+\frac{3}{8}\epsilon\Sigma_i d_t\|\nabla\phi_i\|^2=\underbrace{-\frac{12}{\epsilon}U\int_\Omega H_i\phi_{it}d\boldsymbol{x}}_{\mathrm{IV}_1}-\frac{12}{\epsilon}(\beta,\phi_{it}). \tag{3.14}$$

We multiply (3.5) with $\frac{24}{\epsilon}U$ to derive

$$\frac{12}{\epsilon}d_t|U|^2=\sum_{i=1}^{3}\underbrace{\frac{12}{\epsilon}U\int_\Omega H\phi_{it}d\boldsymbol{x}}_{\mathrm{IV}_2}. \tag{3.15}$$

By multiplying the L^2 inner product of (3.6) with $\mathbf{u}$, we get

$$\frac{1}{2}d_t\|\mathbf{u}\|^2+\nu\|\nabla\mathbf{u}\|^2-(p,\nabla\cdot\mathbf{u})=\underbrace{-Q\sum_{i=1}^{3}\int_\Omega\phi_i\nabla\mu_i\cdot\mathbf{u}d\boldsymbol{x}}_{\mathrm{II}_1}\underbrace{-Q\int_\Omega(\mathbf{u}\cdot\nabla)\mathbf{u}\cdot\mathbf{u}d\boldsymbol{x}}_{\mathrm{III}_1}. \tag{3.16}$$

By multiplying (3.7) with Q, we get

$$d_t\Big(\frac{1}{2}|Q|^2\Big)=\underbrace{Q\sum_{i=1}^{3}\int_\Omega\nabla\cdot(\mathbf{u}\phi_i)\mu_i d\boldsymbol{x}}_{\mathrm{I}_2}+\underbrace{Q\sum_{i=1}^{3}\int_\Omega\phi_i\nabla\mu_i\cdot\mathbf{u}d\boldsymbol{x}}_{\mathrm{II}_2}+\underbrace{Q\int_\Omega\mathbf{u}\cdot\nabla\mathbf{u}\cdot\mathbf{u}d\boldsymbol{x}}_{\mathrm{III}_2}. \tag{3.17}$$

Combining the above five Eqs. (3.13)–(3.17), using $(\beta,\sum_{i=1}^{3}\phi_{it})=(\beta,(1)_t)=0$, and noting that the two terms with the same Rome numerals under curly braces cancel each other out, we derive

$$\begin{aligned}&\frac{d}{dt}E(\mathbf{u},\phi_1,\phi_2,\phi_3,U,Q)\\&\quad=-\nu\|\nabla\mathbf{u}\|^2-M\Big(\Sigma_1\Big\|\frac{\nabla\mu_1}{\Sigma_1}\Big\|^2+\Sigma_2\Big\|\frac{\nabla\mu_2}{\Sigma_2}\Big\|^2+\Sigma_3\Big\|\frac{\nabla\mu_3}{\Sigma_3}\Big\|^2\Big)\\&\quad\le-\nu\|\nabla\mathbf{u}\|^2-M\underline{\Sigma}\Big(\Big\|\frac{\nabla\mu_1}{\Sigma_1}\Big\|^2+\Big\|\frac{\nabla\mu_2}{\Sigma_2}\Big\|^2+\Big\|\frac{\nabla\mu_3}{\Sigma_3}\Big\|^2\Big),\end{aligned} \tag{3.18}$$

where the two negative terms on the right end prescribe the energy diffusive rate and

$$E(\mathbf{u},\phi_1,\phi_2,\phi_3,U,Q)=\frac{1}{2}\|\mathbf{u}\|^2+\frac{3}{8}\epsilon\sum_{i=1}^{3}\Sigma_i\|\nabla\phi_i\|^2+\frac{12}{\epsilon}|U|^2+\frac{1}{2}|Q|^2. \tag{3.19}$$

Remark 3.1. After adding the simple ODE (3.7), we can see that the derivation of the law of energy becomes slightly different from that of the original system. For example, we no longer need the term I_1 in (3.13) and II_1 in (3.16) to cancel each other. Instead, I_1 is canceled by I_2, and II_1 is canceled by II_2, where I_2 and II_2 are from the new ODE (3.7). In other words, for the discrete case, we can use different methods to discretize the advection (associated with I_1) and surface tension (associated with II_1), which makes it possible to design a fully-decoupled scheme.

Now, it is ready to build up a numerical scheme to discretize the new system (3.3)–(3.8) by using the second-order backward differentiation formula (BDF2). It reads as follows.

We compute $(\tilde{\mathbf{u}},\mathbf{u},p,(\phi_i,\mu_i)_{i=1,2,3},U,Q)^{n+1}$ by

$$\frac{a\tilde{\mathbf{u}}^{n+1}-b\mathbf{u}^n+c\mathbf{u}^{n-1}}{2\delta t}+Q^{n+1}(\mathbf{u}^*\cdot\nabla)\mathbf{u}^*-\nu\Delta\tilde{\mathbf{u}}^{n+1}+\nabla p^n+Q^{n+1}\sum_{i=1}^{3}\phi_i^*\nabla\mu_i^*=0, \tag{3.20}$$

$$\frac{a\phi_i^{n+1}-b\phi_i^n+c\phi_i^{n-1}}{2\delta t}+Q^{n+1}\nabla\cdot(\mathbf{u}^*\phi_i^*)=M\Delta\frac{\mu_i^{n+1}}{\Sigma_i}, \tag{3.21}$$

$$\mu_i^{n+1} = -\frac{3}{4}\epsilon\Sigma_i\Delta\phi_i^{n+1} + \frac{12}{\epsilon}(H_i^* + \beta^*)U^{n+1} + \frac{S}{\epsilon}\Sigma_i(\phi_i^{n+1} - \phi_i^*), \tag{3.22}$$

$$aU^{n+1} - bU^n + cU^{n-1} = \frac{1}{2}\sum_{i=1}^{3} H_i^*(a\phi_i^{n+1} - b\phi_i^n + c\phi_i^{n-1}), \tag{3.23}$$

$$\frac{1}{2\delta t}(aQ^{n+1} - bQ^n + cQ^{n-1}) = \sum_{i=1}^{3}\int_\Omega \nabla\cdot(\mathbf{u}^*\phi_i^*)\mu_i^{n+1}d\boldsymbol{x} + \sum_{i=1}^{3}\int_\Omega(\phi_i^*\nabla\mu_i^*)\cdot\tilde{\mathbf{u}}^{n+1}d\boldsymbol{x} + \int_\Omega(\mathbf{u}^*\cdot\nabla)\mathbf{u}^*\cdot\tilde{\mathbf{u}}^{n+1}d\boldsymbol{x}, \tag{3.24}$$

$$\frac{a}{2\delta t}(\mathbf{u}^{n+1} - \tilde{\mathbf{u}}^{n+1}) + \nabla(p^{n+1} - p^n) = 0, \tag{3.25}$$

$$\nabla\cdot\mathbf{u}^{n+1} = 0, \tag{3.26}$$

where

$$\begin{cases} a = 3, b = 4, c = 1,\ \mathbf{u}^* = 2\mathbf{u}^n - \mathbf{u}^{n-1}, \phi_i^* = 2\phi_i^n - \phi_i^{n-1}, \\ \mu_i^* = 2\mu_i^n - \mu_i^{n-1}, H_i^* = H_i(\phi_1^*, \phi_2^*, \phi_3^*), \beta^* = -\dfrac{1}{\Sigma_T}\left(\dfrac{H_1^*}{\Sigma_1} + \dfrac{H_2^*}{\Sigma_2} + \dfrac{H_3^*}{\Sigma_3}\right), \end{cases} \tag{3.27}$$

$S > 0$ is a stabilization parameter, and the boundary conditions of the scheme are either periodic for all variables, or

$$\tilde{\mathbf{u}}^{n+1}|_{\partial\Omega} = \mathbf{u}^{n+1}\cdot\mathbf{n}|_{\partial\Omega} = 0,\ \partial_{\mathbf{n}}\phi_i^{n+1}|_{\partial\Omega} = \partial_{\mathbf{n}}\mu_i^{n+1}|_{\partial\Omega} = 0,\ i = 1, 2, 3. \tag{3.28}$$

In the next few remarks, we give some explanations of the scheme.

Remark 3.2. The scheme is linear and each nonlinear term is discretized using the implicit–explicit combination method. For the hydrodynamical equations, we adopt the second-order pressure-correction scheme (3.20)–(3.25)–(3.26) (cf. [44]) where $\tilde{\mathbf{u}}^{n+1}$ is the intermediate velocity that follows the Dirichlet boundary conditions and the final velocity field $\mathbf{u}^{n+1}$ follows the divergence-free condition. To obtain the pressure, we just apply the divergence operator to (3.25) and then obtain the following Poisson equation for p^{n+1}, i.e.,

$$-\Delta p^{n+1} = -\frac{a}{2\delta t}\nabla\cdot\tilde{\mathbf{u}}^{n+1} - \Delta p^n. \tag{3.29}$$

Once p^{n+1} is computed from (3.29), we update $\mathbf{u}^{n+1}$ by using (3.25), i.e.,

$$\mathbf{u}^{n+1} = \tilde{\mathbf{u}}^{n+1} - \frac{2\delta t}{a}\nabla(p^{n+1} - p^n). \tag{3.30}$$

Remark 3.3. Note that the coefficient H_i^* actually contains explicitly processed terms $f(\phi_1, \phi_2, \phi_3)$, so we add the comparable stabilizer ($S \sim O(1)$) in (3.22). Although this term introduces an extra error of $S\delta t^2\partial_{tt}\phi_i(\cdot)$, whose magnitude is comparable with the error caused by the second-order extrapolated of the nonlinear term $f_i(\phi_1, \phi_2, \phi_3)$. In Section 4, we present enough numerical evidence to show that this stabilizer is critical to maintain the accuracy and improve the energy stability while using large time steps, see the accuracy/stability tests shown in Figs. 4.2 and 4.3.

Remark 3.4. The initialization of the second-order scheme requires all values at $t = t^1$, which can be obtained by constructing the first-order scheme based on the backward Euler method. In the above second-order scheme (3.20)–(3.26), as long as we set $a = 2, b = 2, c = 0$, $\psi^* = \psi^n$ for any variable ψ, the first-order scheme can be easily obtained.

We first prove that the discrete solutions $(\phi_1^{n+1}, \phi_2^{n+1}, \phi_3^{n+1})$ computed by the scheme (3.20)–(3.26) also satisfy the free-leakage condition, i.e., $\phi_1^{n+1} + \phi_2^{n+1} + \phi_3^{n+1} = 1$, that is, there is no volume loss at all time.

Theorem 3.1. *The scheme (3.21)–(3.22) is equivalent to a scheme with two variables as follows:*

$$\frac{a\phi_i^{n+1} - b\phi_i^n + c\phi_i^{n-1}}{2\delta t} + Q^{n+1}\nabla\cdot(\mathbf{u}^*\phi_i^*) = M\Delta\frac{\mu_i^{n+1}}{\Sigma_i}, \tag{3.31}$$

$$\mu_i^{n+1} = -\frac{3}{4}\epsilon\Sigma_i\Delta\phi_i^{n+1} + \frac{12}{\epsilon}(H_i^* + \beta^*)U^{n+1} + \frac{S}{\epsilon}\Sigma_i(\phi_i^{n+1} - \phi_i^*),\ i = 1, 2, \tag{3.32}$$

with

$$\phi_3^{n+1} = 1 - \phi_1^{n+1} - \phi_2^{n+1}, \tag{3.33}$$

$$\frac{\mu_3^{n+1}}{\Sigma_3} = -(\frac{\mu_1^{n+1}}{\Sigma_1} + \frac{\mu_2^{n+1}}{\Sigma_2}). \tag{3.34}$$

Proof. First, we derive (3.21)–(3.22) by assuming that (3.31)–(3.34) are satisfied. Taking the summation of (3.31) for $i = 1, 2$, applying (3.33) at $t = t^{n+1}, t^n, t^{n-1}$, and using (3.34), we obtain

$$\frac{a\phi_3^{n+1} - b\phi_3^n + c\phi_3^{n-1}}{2\delta t} + Q^{n+1}\nabla\cdot(\mathbf{u}^*\phi_3^*) = M\Delta\frac{\mu_3^{n+1}}{\Sigma_3}. \tag{3.35}$$

Furthermore, from (3.34), we derive

$$\begin{aligned}
\mu_3^{n+1} &= -\Sigma_3(\frac{\mu_1^{n+1}}{\Sigma_1} + \frac{\mu_2^{n+1}}{\Sigma_2}) \\
&= -\Sigma_3\Big(-\frac{3}{4}\epsilon\Delta\phi_1^{n+1} - \frac{3}{4}\epsilon\Delta\phi_2^{n+1} + \frac{12}{\epsilon}(\frac{H_1^* + \beta^*}{\Sigma_1} + \frac{H_2^* + \beta^*}{\Sigma_2})U^{n+1} \\
&\quad + \frac{S}{\epsilon}(\phi_1^{n+1} + \phi_2^{n+1} - \phi_1^* - \phi_2^*)\Big) \\
&= -\frac{3}{4}\epsilon\Sigma_3\Delta\phi_3^{n+1} + \frac{12}{\epsilon}(H_3^* + \beta^*)U^{n+1} + \frac{S}{\epsilon}\Sigma_3(\phi_3^{n+1} - \phi_3^*),
\end{aligned}$$

where we use (3.33) and the definition of β^* in (3.27) (that is, $\frac{H_1^*+\beta^*}{\Sigma_1} + \frac{H_2^*+\beta^*}{\Sigma_2} + \frac{H_3^*+\beta^*}{\Sigma_3} = 0$).

Second, we assume that Eqs. (3.21)–(3.22) are satisfied and then derive (3.31)–(3.34). We use the mathematical induction and assume that (3.33) is valid for $t = t^n$ and $t = t^{n-1}$ (the validity of (3.33) at $t = t^1$ can be shown by performing a similar process to the first-order scheme, so the detailed proof is omitted here). For any m, we define

$$C^m = \phi_1^m + \phi_2^m + \phi_3^m,\ \ \Theta^m = \frac{\mu_1^m}{\Sigma_1} + \frac{\mu_2^m}{\Sigma_2} + \frac{\mu_3^m}{\Sigma_3}. \tag{3.36}$$

We take the summation of (3.21) for $i = 1, 2, 3$ to derive

$$\frac{3}{2\delta t}(C^{n+1} - 1) = M\Delta\Theta^{n+1}, \tag{3.37}$$

where the advective terms vanish satisfy $\nabla\cdot(\mathbf{u}^*\sum_{i=1}^3\phi_i^*) = \nabla\cdot\mathbf{u}^* = 0$ since $\sum_{i=1}^3\phi_i^* = 1$ by the induction.

We take the summation of (3.22) for $i = 1, 2, 3$ to get

$$\Theta^{n+1} = -\frac{3}{4}\epsilon\Delta C^{n+1} + \frac{S}{\epsilon}(C^{n+1} - 1). \tag{3.38}$$

Taking the L^2 inner product of (3.37) with $-\frac{2\delta t}{3}\Theta^{n+1}$, of (3.38) with $C^{n+1} - 1$, and summing up the two obtained equalities, we deduce

$$\frac{3}{4}\epsilon\|\nabla C^{n+1}\|^2 + \frac{S}{\epsilon}\|C^{n+1} - 1\|^2 + \frac{2\delta t}{3}M\|\nabla\Theta^{n+1}\|^2 = 0. \tag{3.39}$$

Since all terms on the left hand side of (3.39) are non-negative, thus $\nabla C^{n+1} = 0$ and $\nabla\Theta^{n+1} = 0$ that implies the functions C^{n+1} and Θ^{n+1} are both constants. Then (3.37) leads to $C^{n+1} = 1$ that means the (3.33) is valid. We also derive $\Theta^{n+1} = 0$ from (3.38) that implies (3.34) is valid. □

Here we discuss how to implement the scheme (3.20)–(3.26) in practice. It seems that all unknown variables are nonlocally coupled together, so from the appearance, the scheme (3.20)–(3.26) does not seem to achieve the fully-decoupled structure that we expect. This reminds us that we cannot solve the scheme in any direct ways because doing so will cause a lot of time consumption. Next, we introduce the implementation process in detail, in which we make full use of the nonlocal features of the two additional variables U, Q, as shown below.

First, we use the nonlocal scalar variable Q^{n+1} to split $(\phi_i, \mu_i, U)^{n+1}$ into a linear combination that reads as

$$\begin{cases} \phi_i^{n+1} = \phi_{i,1}^{n+1} + Q^{n+1}\phi_{i,2}^{n+1}, \\ \mu_i^{n+1} = \mu_{i,1}^{n+1} + Q^{n+1}\mu_{i,2}^{n+1}, \\ U^{n+1} = U_1^{n+1} + Q^{n+1}U_2^{n+1}. \end{cases} \tag{3.40}$$

Then the scheme (3.21)–(3.22) can be rewritten as

$$\begin{cases} \dfrac{a}{2\delta t}(\phi_{i,1}^{n+1} + Q^{n+1}\phi_{i,2}^{n+1}) + Q^{n+1}\nabla\cdot(\mathbf{u}^*\phi_i^*) = M\Delta\dfrac{\mu_{i,1}^{n+1} + Q^{n+1}\mu_{i,2}^{n+1}}{\Sigma_i} + \dfrac{b\phi_i^n - c\phi_i^{n-1}}{2\delta t}, \\ \mu_{i,1}^{n+1} + Q^{n+1}\mu_{i,2}^{n+1} = -\dfrac{3}{4}\epsilon\Sigma_i\Delta(\phi_{i,1}^{n+1} + Q^{n+1}\phi_{i,2}^{n+1}) + \dfrac{12}{\epsilon}(H_i^* + \beta^*)(U_1^{n+1} + Q^{n+1}U_2^{n+1}) \\ \qquad\qquad + \dfrac{S}{\epsilon}\Sigma_i(\phi_{i,1}^{n+1} + Q^{n+1}\phi_{i,2}^{n+1} - \phi_i^*). \end{cases} \tag{3.41}$$

According to Q^{n+1}, we split the system (3.41) into two sub-systems as follows,

$$\begin{cases} \dfrac{a}{2\delta t}\phi_{i,1}^{n+1} = M\Delta\dfrac{\mu_{i,1}^{n+1}}{\Sigma_i} + \dfrac{b\phi_i^n - c\phi_i^{n-1}}{2\delta t}, \\ \mu_{i,1}^{n+1} = -\dfrac{3}{4}\epsilon\Sigma_i\Delta\phi_{i,1}^{n+1} + \dfrac{12}{\epsilon}(H_i^* + \beta^*)U_1^{n+1} + \dfrac{S}{\epsilon}\Sigma_i(\phi_{i,1}^{n+1} - \phi_i^*), \end{cases} \tag{3.42}$$

$$\begin{cases} \dfrac{a}{2\delta t}\phi_{i,2}^{n+1} = M\Delta\dfrac{\mu_{i,2}^{n+1}}{\Sigma_i} - \nabla\cdot(\mathbf{u}^*\phi_i^*), \\ \mu_{i,2}^{n+1} = -\dfrac{3}{4}\epsilon\Sigma_i\Delta\phi_{i,2}^{n+1} + \dfrac{12}{\epsilon}(H_i^* + \beta^*)U_2^{n+1} + \dfrac{S}{\epsilon}\Sigma_i\phi_{i,2}^{n+1}. \end{cases} \tag{3.43}$$

By applying procedures similar to the second-step proof in Theorem 3.1 to the two systems (3.42) and (3.43), we derive

$$\begin{cases} \phi_{1,1}^{n+1} + \phi_{2,1}^{n+1} + \phi_{3,1}^{n+1} = 1, \\ \dfrac{\mu_{1,1}^{n+1}}{\Sigma_i} + \dfrac{\mu_{2,1}^{n+1}}{\Sigma_2} + \dfrac{\mu_{3,1}^{n+1}}{\Sigma_3} = 0, \\ \phi_{1,2}^{n+1} + \phi_{2,2}^{n+1} + \phi_{3,2}^{n+1} = 0, \\ \dfrac{\mu_{1,2}^{n+1}}{\Sigma_i} + \dfrac{\mu_{2,2}^{n+1}}{\Sigma_2} + \dfrac{\mu_{3,2}^{n+1}}{\Sigma_3} = 0. \end{cases} \tag{3.44}$$

Note that the two subsystems (3.42) and (3.43) have the same form, so we only need to introduce the method to solve any of them, and the other follows the same line. Hence, we take the first subsystem (3.42) as an example. To solve it, we continue to use the split technique, that is, the variables $(\phi_{i,1}, \mu_{i,1})^{n+1}$ are split into a linear combination form by the nonlocal variable U_1^{n+1}, which reads as

$$\begin{cases} \phi_{i,1}^{n+1} = \phi_{i,1,1}^{n+1} + U_1^{n+1}\phi_{i,1,2}^{n+1}, \\ \mu_{i,1}^{n+1} = \mu_{i,1,1}^{n+1} + U_1^{n+1}\mu_{i,1,2}^{n+1}. \end{cases} \tag{3.45}$$

By substituting the split form of all variables in (3.45) into (3.42) and decomposing the results according to the nonlocal variable U_1^{n+1}, we obtain the following independent subsystems that read as

$$\begin{cases} \dfrac{a}{2\delta t}\phi_{i,1,1}^{n+1} = M\Delta\dfrac{\mu_{i,1,1}^{n+1}}{\Sigma_i} + \dfrac{b\phi_i^n - c\phi_i^{n-1}}{2\delta t}, \\ \mu_{i,1,1}^{n+1} = -\dfrac{3}{4}\epsilon\Sigma_i\Delta\phi_{i,1,1}^{n+1} + \dfrac{S}{\epsilon}\Sigma_i(\phi_{i,1,1}^{n+1} - \phi_i^*), \end{cases} \tag{3.46}$$

$$\begin{cases} \dfrac{a}{2\delta t}\phi_{i,1,2}^{n+1} = M\Delta\dfrac{\mu_{i,1,2}^{n+1}}{\Sigma_i}, \\ \mu_{i,1,2}^{n+1} = -\dfrac{3}{4}\epsilon\Sigma_i\Delta\phi_{i,1,2}^{n+1} + \dfrac{12}{\epsilon}(H_i^* + \beta^*) + \dfrac{S}{\epsilon}\Sigma_i\phi_{i,1,2}^{n+1}. \end{cases} \tag{3.47}$$

The boundary conditions for (3.46)–(3.47) are either periodic or

$$\partial_{\mathbf{n}}(\phi_{i,1,1}, \phi_{i,1,2}, \mu_{i,1,1}, \mu_{i,1,2})^{n+1}|_{\partial\Omega} = 0. \tag{3.48}$$

We can directly solve $(\phi_{i,1,1}, \phi_{i,1,2}, \mu_{i,1,1}, \mu_{i,1,2})^{n+1}$, $i = 1, 2, 3$ from the above sub-systems (3.46)–(3.47) since all nonlinear terms are given explicitly; or we can solve (3.46)–(3.47) for $i = 1, 2$ and update $i = 3$ from the following conditions

$$\begin{cases} \phi_{1,1,1}^{n+1} + \phi_{2,1,1}^{n+1} + \phi_{3,1,1}^{n+1} = 1, & \dfrac{\mu_{1,1,1}^{n+1}}{\Sigma_i} + \dfrac{\mu_{2,1,1}^{n+1}}{\Sigma_2} + \dfrac{\mu_{3,1,1}^{n+1}}{\Sigma_3} = 0, \\ \phi_{1,1,2}^{n+1} + \phi_{2,1,2}^{n+1} + \phi_{3,1,2}^{n+1} = 0, & \dfrac{\mu_{1,1,2}^{n+1}}{\Sigma_i} + \dfrac{\mu_{2,1,2}^{n+1}}{\Sigma_2} + \dfrac{\mu_{3,1,2}^{n+1}}{\Sigma_3} = 0, \end{cases} \tag{3.49}$$

which can be easily obtained from (3.46)–(3.47) by performing a derivation process similar to the proof of the second step of Theorem 3.1.

For the system (3.43), we implement it in a similar way. By splitting $(\phi_{i,2}, \mu_{i,2})^{n+1}$ into the following linear combination form by the nonlocal variable U_2^{n+1}, i.e.,

$$\begin{cases} \phi_{i,2}^{n+1} = \phi_{i,2,1}^{n+1} + U_2^{n+1}\phi_{i,2,2}^{n+1}, \\ \mu_{i,2}^{n+1} = \mu_{i,2,1}^{n+1} + U_2^{n+1}\mu_{i,2,2}^{n+1}. \end{cases} \tag{3.50}$$

Then the unknowns $(\phi_{i,2,1}, \phi_{i,2,2}, \mu_{i,2,1}, \mu_{i,2,2})^{n+1}$ can be obtained by solving another several sub-systems that are similar to (3.46)–(3.47) with the same boundary conditions specified as (3.48).

Second, we rewrite (3.23) as the following form

$$U^{n+1} = \frac{1}{2}\sum_{i=1}^{3}\int_{\Omega} H_i^*\phi_i^{n+1}d\boldsymbol{x} + g^n, \tag{3.51}$$

where $g^n = \frac{1}{a}(bU^n - cU^{n-1}) - \frac{1}{2a}\sum_{i=1}^{3}\int_{\Omega} H_i^*(b\phi_i^n - c\phi_i^{n-1})d\boldsymbol{x}$ is the explicit form. By substituting the linear form of (U, ϕ_i^{n+1}) represented by Q^{n+1} given in (3.40) into (3.51), we obtain

$$U_1^{n+1} + Q^{n+1}U_2^{n+1} = \frac{1}{2}\sum_{i=1}^{3}\int_{\Omega} H_i^*(\phi_{i,1}^{n+1} + Q^{n+1}\phi_{i,2}^{n+1})d\boldsymbol{x} + g^n. \tag{3.52}$$

Then, according to Q^{n+1}, we decompose (3.52) into the following two equalities:

$$\begin{cases} U_1^{n+1} = \dfrac{1}{2}\displaystyle\sum_{i=1}^{3}\int_{\Omega} H_i^*\phi_{i,1}^{n+1}d\boldsymbol{x} + g^n, \\ U_2^{n+1} = \dfrac{1}{2}\displaystyle\sum_{i=1}^{3}\int_{\Omega} H_i^*\phi_{i,2}^{n+1}d\boldsymbol{x}. \end{cases} \tag{3.53}$$

Substituting the linear form of $(\phi_{i,1}, \phi_{i,2})^{n+1}$ given in (3.45) and (3.50) into (3.53), we get

$$\begin{cases} U_1^{n+1} = \dfrac{1}{2}\displaystyle\sum_{i=1}^{3}\int_{\Omega} H_i^*(\phi_{i,1,1}^{n+1} + U_1^{n+1}\phi_{i,1,2}^{n+1})d\boldsymbol{x} + g^n, \\ U_2^{n+1} = \dfrac{1}{2}\displaystyle\sum_{i=1}^{3}\int_{\Omega} H_i^*(\phi_{i,2,1}^{n+1} + U_2^{n+1}\phi_{i,2,2}^{n+1})d\boldsymbol{x}. \end{cases} \tag{3.54}$$

After applying a simple factorization to (3.54), we derive

$$\begin{cases} U_1^{n+1} = \dfrac{\frac{1}{2}\sum_{i=1}^{3}\int_{\Omega} H_i^*\phi_{i,1,1}^{n+1}d\boldsymbol{x} + g^n}{1 - \frac{1}{2}\sum_{i=1}^{3}\int_{\Omega} H_i^*\phi_{i,1,2}^{n+1}d\boldsymbol{x}}, \\ U_2^{n+1} = \dfrac{\frac{1}{2}\sum_{i=1}^{3}\int_{\Omega} H_i^*\phi_{i,2,1}^{n+1}d\boldsymbol{x}}{1 - \frac{1}{2}\sum_{i=1}^{3}\int_{\Omega} H_i^*\phi_{i,2,2}^{n+1}d\boldsymbol{x}}. \end{cases} \tag{3.55}$$

An important thing is to verify whether U_1^{n+1} and U_2^{n+1} are solvable. This can be obtained by applying simple energy estimation to the subsystem (3.47). For any $\psi \in L^2(\Omega)$ with $\int_\Omega \psi d\boldsymbol{x} = 0$, we define $\phi = \Delta^{-1}\psi$ to be the solution of the following Poisson equation

$$\Delta\phi = \psi, \int_\Omega \phi d\boldsymbol{x} = 0, \tag{3.56}$$

where the boundary condition is decided by the system (i.e., if the system is with periodic boundary condition, then ψ is periodic; if the system is with the boundary condition described in (2.19), then $\partial_{\mathbf{n}}\phi|_{\partial\Omega} = 0$.)

By applying Δ^{-1} to the first equation of (3.47) and combine the obtained result with the second equation of (3.47), we obtain

$$\frac{a}{2M\delta t}\Delta^{-1}\phi_{i,1,2}^{n+1} = -\frac{3}{4}\epsilon\Sigma_i\Delta\phi_{i,1,2}^{n+1} + \frac{12}{\epsilon}(H_i^* + \beta^*) + \frac{S}{\epsilon}\Sigma_i\phi_{i,1,2}. \tag{3.57}$$

By taking the L^2 inner product of (3.57) with $\phi_{i,1,2}^{n+1}$ and taking the summation for $i = 1, 2, 3$, we derive

$$\begin{aligned} -\frac{12}{\epsilon}\sum_{i=1}^{3}\int_\Omega H_i^*\phi_{i,1,2}^{n+1}d\boldsymbol{x} =& \frac{a}{2M\delta t}\sum_{i=1}^{3}\|\nabla\Delta^{-1}\phi_{i,1,2}^{n+1}\|^2 + \frac{3}{4}\epsilon\sum_{i=1}^{3}\Sigma_i\|\nabla\phi_{i,1,2}\|^2 \\ &+ \frac{S}{\epsilon}\sum_{i=1}^{3}\Sigma_i\|\phi_{i,1,2}^{n+1}\|^2 + \sum_{i=1}^{3}(\beta^*, \phi_{i,1,2}^{n+1}) \geq 0, \end{aligned} \tag{3.58}$$

where the term $\sum_{i=1}^{3}(\beta^*, \phi_{i,1,2}^{n+1}) = 0$ due to (3.49). Hence U_1^{n+1} is uniquely solvable. By performing similar energy estimation on the two sub-systems split from (3.43) (according to U_2^{n+1}), it can be easily shown that U_2^{n+1} is also uniquely solvable. After calculating U_1^{n+1} and U_2^{n+1} from (3.55), we further obtain $\phi_{i,1}^{n+1}$, $\mu_{i,1}^{n+1}$ from (3.45), and $\phi_{i,2}^{n+1}$, $\mu_{i,2}^{n+1}$ from (3.50).

Third, for the velocity field $\tilde{\mathbf{u}}^{n+1}, \mathbf{u}^{n+1}$ and the pressure p^{n+1} in the scheme (3.20) and (3.25)–(3.26), we also use the nonlocal variable Q^{n+1} to split them as the following linear combinations:

$$\begin{cases} \tilde{\mathbf{u}}^{n+1} = \tilde{\mathbf{u}}_1^{n+1} + Q^{n+1}\tilde{\mathbf{u}}_2^{n+1}, \\ \mathbf{u}^{n+1} = \mathbf{u}_1^{n+1} + Q^{n+1}\mathbf{u}_2^{n+1}, \\ p^{n+1} = p_1^{n+1} + Q^{n+1}p_2^{n+1}. \end{cases} \tag{3.59}$$

In the scheme (3.20) and (3.25)–(3.26), using (3.59) to replace the variables $(\tilde{\mathbf{u}}, \mathbf{u}, p)^{n+1}$ and then splitting the obtained equations according to Q^{n+1}, we obtain several sub-equations, which can be solved independently. More precisely, starting with (3.20), the two split variables $\tilde{\mathbf{u}}_1^{n+1}$ and $\tilde{\mathbf{u}}_2^{n+1}$ satisfy the following equations:

$$\begin{cases} \frac{a}{2\delta t}\tilde{\mathbf{u}}_1^{n+1} - \nu\Delta\tilde{\mathbf{u}}_1^{n+1} = \sigma_1, \\ \frac{a}{2\delta t}\tilde{\mathbf{u}}_2^{n+1} - \nu\Delta\tilde{\mathbf{u}}_2^{n+1} = \sigma_2, \end{cases} \tag{3.60}$$

where σ_1, σ_2 are explicit forms that are given by

$$\begin{cases} \sigma_1 = -\nabla p^n + \dfrac{b\mathbf{u}^n - c\mathbf{u}^{n-1}}{2\delta t}, \\ \sigma_2 = -(\mathbf{u}^* \cdot \nabla)\mathbf{u}^* - \displaystyle\sum_{i=1}^{3}\phi_i^*\nabla\mu_i^*. \end{cases} \tag{3.61}$$

For (3.25)–(3.26), using the two split variables $\mathbf{u}_i^{n+1}, p_i^{n+1}, i = 1, 2$, we obtain

$$\begin{cases} \frac{a}{2\delta t}(\mathbf{u}_1^{n+1} - \tilde{\mathbf{u}}_1^{n+1}) + \nabla p_1^{n+1} = \nabla p^n, \quad \nabla \cdot \mathbf{u}_1^{n+1} = 0, \\ \frac{a}{2\delta t}(\mathbf{u}_2^{n+1} - \tilde{\mathbf{u}}_2^{n+1}) + \nabla p_2^{n+1} = 0, \qquad \nabla \cdot \mathbf{u}_2^{n+1} = 0. \end{cases} \tag{3.62}$$

We require four split variables $\tilde{\mathbf{u}}_i^{n+1}, \mathbf{u}_i^{n+1}, i = 1, 2$ follow the boundary conditions described in (3.28), i.e., they are either periodic or satisfy:

$$\tilde{\mathbf{u}}_i^{n+1}|_{\partial\Omega} = \mathbf{u}_i^{n+1} \cdot \mathbf{n}|_{\partial\Omega} = 0. \tag{3.63}$$

Fourth, we solve the auxiliary variable Q^{n+1}. Using the split form for the variables μ_i^{n+1} in (3.40) and $\tilde{\mathbf{u}}^{n+1}$ in (3.59), one can rewrite (3.24) as the following form:

$$(\frac{a}{2\delta t} - \vartheta_2)Q^{n+1} = \frac{1}{2\delta t}(bQ^n - cQ^{n-1}) + \vartheta_1, \tag{3.64}$$

where $\vartheta_i, i = 1, 2$ are given as:

$$\begin{cases} \vartheta_1 = \sum_{i=1}^{3}\int_\Omega \nabla\cdot(\mathbf{u}^*\phi_i^*)\mu_{i,1}^{n+1}d\boldsymbol{x} + \sum_{i=1}^{3}\int_\Omega(\phi_i^*\nabla\mu_i^*)\cdot\tilde{\mathbf{u}}_1^{n+1}d\boldsymbol{x} + \int_\Omega(\mathbf{u}^*\cdot\nabla)\mathbf{u}^*\cdot\tilde{\mathbf{u}}_1^{n+1}d\boldsymbol{x}, \\ \vartheta_2 = \sum_{i=1}^{3}\int_\Omega \nabla\cdot(\mathbf{u}^*\phi_i^*)\mu_{i,2}^{n+1}d\boldsymbol{x} + \sum_{i=1}^{3}\int_\Omega(\phi_i^*\nabla\mu_i^*)\cdot\tilde{\mathbf{u}}_2^{n+1}d\boldsymbol{x} + \int_\Omega(\mathbf{u}^*\cdot\nabla)\mathbf{u}^*\cdot\tilde{\mathbf{u}}_2^{n+1}d\boldsymbol{x}. \end{cases} \tag{3.65}$$

We need to verify (3.64) is solvable. By taking the L^2 inner product of the second equation in (3.60) with $\tilde{\mathbf{u}}_2^{n+1}$, we derive

$$-\int_\Omega(\mathbf{u}^*\cdot\nabla)\mathbf{u}^*\cdot\tilde{\mathbf{u}}_2^{n+1}d\boldsymbol{x} - \sum_{i=1}^{3}\int_\Omega(\phi_i^*\nabla\mu_i^*)\cdot\tilde{\mathbf{u}}_2^{n+1}d\boldsymbol{x} = \frac{a}{2\delta t}\|\tilde{\mathbf{u}}_2^{n+1}\|^2 + \nu\|\nabla\tilde{\mathbf{u}}_2^{n+1}\|^2 \geq 0. \tag{3.66}$$

We further take the L^2 inner product of the first equation in (3.43) with $\mu_{i,2}^{n+1}$ to get

$$-\int_\Omega\nabla\cdot(\mathbf{u}^*\phi_i^*)\mu_{i,2}^{n+1}d\boldsymbol{x} = M\Sigma_i\left\|\frac{\mu_{i,2}^{n+1}}{\Sigma_i}\right\|^2 + \frac{a}{2\delta t}(\phi_{i,2}^{n+1}, \mu_{i,2}^{n+1}), \tag{3.67}$$

and of the second equation in (3.43) with $\frac{a}{2\delta t}\phi_{i,2}^{n+1}$ to get

$$\begin{aligned} \frac{a}{2\delta t}(\phi_{i,2}^{n+1}, \mu_{i,2}^{n+1}) =& \frac{3a}{8\delta t}\epsilon\Sigma_i\|\nabla\phi_{i,2}^{n+1}\|^2 + \frac{aS}{2\delta t\epsilon}\Sigma_i\|\phi_{i,2}^{n+1}\|^2 \\ &+ \frac{12a}{2\delta t\epsilon}U_2^{n+1}\int_\Omega H_i^*\phi_{i,2}^{n+1}d\boldsymbol{x} + \frac{12a}{2\delta t\epsilon}U_2^{n+1}(\beta, \phi_{i,2}^{n+1}). \end{aligned} \tag{3.68}$$

Combining (3.67) and (3.68) and taking the summation for $i = 1, 2, 3$, we derive

$$\begin{aligned} -\sum_{i=1}^{3}\int_\Omega\nabla\cdot(\mathbf{u}^*\phi_i^*)\mu_{i,2}^{n+1}d\boldsymbol{x} =& M\sum_{i=1}^{3}\Sigma_i\left\|\frac{\mu_{i,2}^{n+1}}{\Sigma_i}\right\|^2 + \frac{3a}{8\delta t}\epsilon\sum_{i=1}^{3}\Sigma_i\|\nabla\phi_{i,2}^{n+1}\|^2 \\ &+ \frac{aS}{2\delta t\epsilon}\sum_{i=1}^{3}\Sigma_i\|\phi_{i,2}^{n+1}\|^2 + \frac{12a}{2\delta t\epsilon}U_2^{n+1}(\beta, \sum_{i=1}^{3}\phi_{i,2}^{n+1}) \\ &+ \frac{12a}{2\delta t\epsilon}U_2^{n+1}\sum_{i=1}^{3}\int_\Omega H_i^*\phi_{i,2}^{n+1}d\boldsymbol{x}. \end{aligned} \tag{3.69}$$

By using the third and fourth equality of (3.44) and applying (2.9), we derive

$$\begin{aligned} &\sum_{i=1}^{3}\Sigma_i\left\|\frac{\mu_{i,2}^{n+1}}{\Sigma_i}\right\|^2 \geq \underline{\Sigma}\sum_{i=1}^{3}\left\|\frac{\mu_{i,2}^{n+1}}{\Sigma_i}\right\|^2 \geq 0, \qquad \sum_{i=1}^{3}\Sigma_i\|\nabla\phi_{i,2}^{n+1}\|^2 \geq \underline{\Sigma}\sum_{i=1}^{3}\|\nabla\phi_{i,2}^{n+1}\|^2 \geq 0, \\ &\sum_{i=1}^{3}\Sigma_i\|\phi_{i,2}^{n+1}\|^2 \geq \underline{\Sigma}\sum_{i=1}^{3}\|\phi_{i,2}^{n+1}\|^2 \geq 0, \qquad (\beta, \sum_{i=1}^{3}\phi_{i,2}^{n+1}) = 0. \end{aligned} \tag{3.70}$$

From the second equation of (3.53), we derive

$$U_2^{n+1}\sum_{i=1}^{3}\int_\Omega H_i^*\phi_{i,2}^{n+1}d\boldsymbol{x} = \frac{1}{2}\left(\sum_{i=1}^{3}\int_\Omega H_i^*\phi_{i,2}^{n+1}d\boldsymbol{x}\right)^2 \geq 0. \tag{3.71}$$

Hence we have

$$-\sum_{i=1}^{3}\int_{\Omega}\nabla\cdot(\mathbf{u}^{*}\phi^{*})\mu_{i,2}^{n+1}d\boldsymbol{x}\geq 0. \tag{3.72}$$

Therefore, (3.66) and (3.72) imply that $-\vartheta_2\geq 0$, thereby ensuring the solvability of (3.64).

Finally, we update ϕ_i^{n+1}, μ_i^{n+1} for $i=1,2,3$ and U^{n+1} from (3.40), $\tilde{\mathbf{u}}^{n+1}$, $\mathbf{u}^{n+1}$, and p^{n+1} from (3.59).

We summarize the implementation of scheme (3.20)–(3.26) as follows:

- **Step 1**: Compute $(\phi_{i,1,1},\,\phi_{i,1,2},\,\mu_{i,1,1},\,\mu_{i,1,2})^{n+1}$ for $i=1,2,3$ from (3.46)–(3.47), and compute $(\phi_{i,2,1},\,\phi_{i,2,2},\,\mu_{i,2,1},\,\mu_{i,2,2})^{n+1}$ for $i=1,2,3$ from another similar two sub-systems split from (3.43) using the variable U_2^{n+1};
- **Step 2**: Update U_1^{n+1}, U_2^{n+1} from (3.55);
- **Step 3**: Update $(\phi_{i,1},\,\mu_{i,1})^{n+1}$ for $i=1,2,3$ from (3.45), and update $(\phi_{i,2},\,\mu_{i,2})^{n+1}$ for $i=1,2,3$ from (3.50);
- **Step 4**: Compute $\tilde{\mathbf{u}}_i^{n+1}$, $i=1,2$ from (3.60);
- **Step 5**: Compute $\mathbf{u}_i^{n+1}$ and p_i^{n+1}, $i=1,2$ from (3.62);
- **Step 6**: Compute Q^{n+1} from (3.64);
- **Step 7**: Update ϕ_i^{n+1}, μ_i^{n+1} for $i=1,2,3$ and U^{n+1} from (3.40), and update $\tilde{\mathbf{u}}^{n+1}$, $\mathbf{u}^{n+1}$, and p^{n+1} from (3.59).

Therefore, if third phase-field variable is always updated by using the relationship of the three phases (for instance, (3.44), (3.49)), then the total computational cost needed by the scheme (3.20)–(3.26) at each time step includes solving four independent elliptic linear systems in Step 1, two elliptic equations in Step 4, and two more Poisson type equations in Step 5. All these equations have constant coefficients and are fully-decoupled, which means very efficient calculations in practice.

Now the energy stability of the developed scheme (3.20)–(3.26) is shown as follows.

Theorem 3.2. *The following discrete energy dissipation law holds for the scheme (3.20)–(3.26),*

$$\frac{1}{\delta t}(E^{n+1}-E^{n})\leq-\nu\|\nabla\tilde{\mathbf{u}}^{n+1}\|^{2}-M\Sigma\sum_{i=1}^{3}\left\|\frac{\nabla\mu_i^{n+1}}{\Sigma_i}\right\|^{2}\leq 0, \tag{3.73}$$

where

$$\begin{aligned}E^{n+1}=&\frac{1}{2}\Big(\frac{1}{2}\|\mathbf{u}^{n+1}\|^{2}+\frac{1}{2}\|2\mathbf{u}^{n+1}-\mathbf{u}^{n}\|^{2}\Big)+\frac{\delta t^{2}}{3}\|\nabla p^{n+1}\|^{2}\\&+\frac{3\epsilon}{8}\sum_{i=1}^{3}\Big(\Sigma_i(\frac{1}{2}\|\nabla\phi_i^{n+1}\|^{2}+\frac{1}{2}\|2\nabla\phi_i^{n+1}-\nabla\phi_i^{n}\|^{2})\Big)\\&+\frac{12}{\epsilon}\Big(\frac{1}{2}|U^{n+1}|^{2}+\frac{1}{2}|2U^{n+1}-U^{n}|^{2}\Big)+\frac{1}{2}\Big(\frac{1}{2}|Q^{n+1}|^{2}+\frac{1}{2}|2Q^{n+1}-Q^{n}|^{2}\Big)\\&+\frac{S}{2\epsilon}\sum_{i=1}^{3}(\Sigma_i\|\phi_i^{n+1}-\phi_i^{n}\|^{2})\geq 0.\end{aligned} \tag{3.74}$$

Proof. We multiply the inner product of (3.20) with $2\delta t\tilde{\mathbf{u}}^{n+1}$ in the L^2 space to get

$$\begin{aligned}&(3\tilde{\mathbf{u}}^{n+1}-4\mathbf{u}^{n}+\mathbf{u}^{n-1},\tilde{\mathbf{u}}^{n+1})+2\nu\delta t\|\nabla\tilde{\mathbf{u}}^{n+1}\|^{2}+2\delta t(\nabla p^{n},\tilde{\mathbf{u}}^{n+1})\\&\quad=-2\delta t\,Q^{n+1}\int_{\Omega}(\mathbf{u}^{*}\cdot\nabla)\mathbf{u}^{*}\cdot\tilde{\mathbf{u}}^{n+1}d\boldsymbol{x}-2\delta t\,Q^{n+1}\sum_{i=1}^{3}\int_{\Omega}(\phi_i^{*}\nabla\mu_i^{*})\cdot\tilde{\mathbf{u}}^{n+1}d\boldsymbol{x}.\end{aligned} \tag{3.75}$$

From (3.25), for any variable $\mathbf{v}$ with $\nabla\cdot\mathbf{v}=0$, we have

$$(\mathbf{u}^{n+1},\mathbf{v})=(\tilde{\mathbf{u}}^{n+1},\mathbf{v}). \tag{3.76}$$

We derive following equality

$$\begin{aligned}
&(3\tilde{\mathbf{u}}^{n+1}-4\mathbf{u}^{n}+\mathbf{u}^{n-1},\tilde{\mathbf{u}}^{n+1})\\
&\quad=(3\tilde{\mathbf{u}}^{n+1}-4\mathbf{u}^{n}+\mathbf{u}^{n-1},\mathbf{u}^{n+1})+(3\tilde{\mathbf{u}}^{n+1}-4\mathbf{u}^{n}+\mathbf{u}^{n-1},\tilde{\mathbf{u}}^{n+1}-\mathbf{u}^{n+1})\\
&\quad=(3\mathbf{u}^{n+1}-4\mathbf{u}^{n}+\mathbf{u}^{n-1},\mathbf{u}^{n+1})+(3\tilde{\mathbf{u}}^{n+1},\ \tilde{\mathbf{u}}^{n+1}-\mathbf{u}^{n+1})\\
&\quad=(3\mathbf{u}^{n+1}-4\mathbf{u}^{n}+\mathbf{u}^{n-1},\mathbf{u}^{n+1})+3(\tilde{\mathbf{u}}^{n+1}-\mathbf{u}^{n+1},\tilde{\mathbf{u}}^{n+1}+\mathbf{u}^{n+1})\\
&\quad=\frac{1}{2}\Big(\|\mathbf{u}^{n+1}\|^2-\|\mathbf{u}^{n}\|^2+\|2\mathbf{u}^{n+1}-\mathbf{u}^{n}\|^2-\|2\mathbf{u}^{n}-\mathbf{u}^{n-1}\|^2\\
&\qquad+\|\mathbf{u}^{n+1}-2\mathbf{u}^{n}+\mathbf{u}^{n-1}\|^2\Big)+3(\|\tilde{\mathbf{u}}^{n+1}\|^2-\|\mathbf{u}^{n+1}\|^2),
\end{aligned}\tag{3.77}$$

where we use the following identity

$$2(3a-4b+c,a)=a^2-b^2+(2a-b)^2-(2b-c)^2+(a-2b+c)^2.\tag{3.78}$$

We reformulate the projection step (3.25) as

$$\frac{3}{2\delta t}\mathbf{u}^{n+1}+\nabla p^{n+1}=\frac{3}{2\delta t}\tilde{\mathbf{u}}^{n+1}+\nabla p^{n}.\tag{3.79}$$

By taking the square of both sides of the above equation, we get

$$\frac{9}{4\delta t^2}\|\mathbf{u}^{n+1}\|^2+\|\nabla p^{n+1}\|^2=\frac{9}{4\delta t^2}\|\tilde{\mathbf{u}}^{n+1}\|^2+\|\nabla p^{n}\|^2+\frac{3}{\delta t}(\tilde{\mathbf{u}}^{n+1},\nabla p^{n}).\tag{3.80}$$

Hence, by multiplying $2\delta t^2/3$ of the above equation, we derive

$$\frac{3}{2}(\|\mathbf{u}^{n+1}\|^2-\|\tilde{\mathbf{u}}^{n+1}\|^2)+\frac{2\delta t^2}{3}(\|\nabla p^{n+1}\|^2-\|\nabla p^{n}\|^2)=2\delta t(\tilde{\mathbf{u}}^{n+1},\nabla p^{n}).\tag{3.81}$$

By taking the inner product of (3.25) with $2\delta t\mathbf{u}^{n+1}$ in the L^2 space, we have

$$\frac{3}{2}(\|\mathbf{u}^{n+1}\|^2-\|\tilde{\mathbf{u}}^{n+1}\|^2+\|\mathbf{u}^{n+1}-\tilde{\mathbf{u}}^{n+1}\|^2)=0.\tag{3.82}$$

We combine (3.75), (3.77), (3.81), and (3.82) to obtain

$$\begin{aligned}
&\frac{1}{2}(\|\mathbf{u}^{n+1}\|^2-\|\mathbf{u}^{n}\|^2+\|2\mathbf{u}^{n+1}-\mathbf{u}^{n}\|^2-\|2\mathbf{u}^{n}-\mathbf{u}^{n-1}\|^2+\|\mathbf{u}^{n+1}-2\mathbf{u}^{n}+\mathbf{u}^{n-1}\|^2)\\
&\qquad+\frac{3}{2}\|\mathbf{u}^{n+1}-\tilde{\mathbf{u}}^{n+1}\|^2+\frac{2\delta t^2}{3}(\|\nabla p^{n+1}\|^2-\|\nabla p^{n}\|^2)+2\nu\delta t\|\nabla\tilde{\mathbf{u}}^{n+1}\|^2\\
&\qquad=-2\delta t\,Q^{n+1}\int_\Omega(\mathbf{u}^*\cdot\nabla)\mathbf{u}^*\cdot\tilde{\mathbf{u}}^{n+1}d\boldsymbol{x}-2\delta t\,Q^{n+1}\sum_{i=1}^{3}\int_\Omega(\phi_i^*\nabla\mu_i^*)\cdot\tilde{\mathbf{u}}^{n+1}d\boldsymbol{x}.
\end{aligned}\tag{3.83}$$

Computing the inner product of (3.21) with $2\delta t\mu_i^{n+1}$ in the L^2 space, we have

$$(3\phi_i^{n+1}-4\phi_i^{n}+\phi_i^{n-1},\mu_i^{n+1})+2\delta t\,M\Sigma_i\left\|\frac{\nabla\mu_i^{n+1}}{\Sigma_i}\right\|^2=-2\delta t\,Q^{n+1}\int_\Omega\nabla\cdot(\mathbf{u}^*\phi_i^*)\mu_i^{n+1}d\boldsymbol{x}.\tag{3.84}$$

Computing the L^2 inner product of (3.22) with $-(3\phi^{n+1}-4\phi^{n}+\phi^{n-1})$, we find

$$\begin{aligned}
&-(\mu_i^{n+1},3\phi_i^{n+1}-4\phi_i^{n}+\phi_i^{n-1})+\frac{3}{4}\epsilon\Sigma_i(\nabla\phi_i^{n+1},\nabla(3\phi_i^{n+1}-4\phi_i^{n}+\phi_i^{n-1}))\\
&\qquad=-\frac{12}{\epsilon}U^{n+1}\int_\Omega(H_i^*+\beta^*)(3\phi_i^{n+1}-4\phi_i^{n}+\phi_i^{n-1})d\boldsymbol{x}\\
&\qquad\quad-\frac{S}{\epsilon}(\Sigma_i(\phi_i^{n+1}-\phi_i^*),3\phi_i^{n+1}-4\phi_i^{n}+\phi_i^{n-1}).
\end{aligned}\tag{3.85}$$

We multiply (3.23) with $\frac{24}{\epsilon}U^{n+1}$ and use (3.78) to obtain

$$\begin{aligned}\frac{12}{\epsilon}\Big(|U^{n+1}|^2-|U^n|^2+|2U^{n+1}-U^n|^2-|2U^n-U^{n-1}|^2+|U^{n+1}-2U^n+U^{n-1}|^2\Big)\\ =\frac{12}{\epsilon}\sum_{i=1}^{3}U^{n+1}\int_\Omega H_i^*(3\phi_i^{n+1}-4\phi_i^n+\phi_i^{n-1})d\boldsymbol{x}.\end{aligned}\tag{3.86}$$

We multiply (3.24) with $2\delta t\,Q^{n+1}$ and use (3.78) to obtain

$$\begin{aligned}\frac{1}{2}\Big(|Q^{n+1}|^2-|Q^n|^2+|2Q^{n+1}-Q^n|^2-|2Q^n-Q^{n-1}|^2+|Q^{n+1}-2Q^n+Q^{n-1}|^2\Big)\\ =2\delta t\,Q^{n+1}\sum_{i=1}^{3}\int_\Omega\nabla\cdot(\mathbf{u}^*\phi_i^*)\mu_i^{n+1}d\boldsymbol{x}+2\delta t\,Q^{n+1}\sum_{i=1}^{3}\int_\Omega(\phi_i^*\nabla\mu_i^*)\cdot\tilde{\mathbf{u}}^{n+1}d\boldsymbol{x}\\ +2\delta t\,Q^{n+1}\int_\Omega(\mathbf{u}^*\cdot\nabla)\mathbf{u}^*\cdot\tilde{\mathbf{u}}^{n+1}d\boldsymbol{x}.\end{aligned}\tag{3.87}$$

Hence, by combining (3.83)–(3.87) and taking the summation for $i=1,2,3$, we arrive at

$$\begin{aligned}&\frac{1}{2}(\|\mathbf{u}^{n+1}\|^2-\|\mathbf{u}^n\|^2+\|2\mathbf{u}^{n+1}-\mathbf{u}^n\|^2-\|2\mathbf{u}^n-\mathbf{u}^{n-1}\|^2)+\frac{2\delta t^2}{3}(\|\nabla p^{n+1}\|^2-\|\nabla p^n\|^2)\\ &+\frac{3\epsilon}{8}\sum_{i=1}^{3}\Big(\Sigma_i(\|\nabla\phi_i^{n+1}\|^2-\|\nabla\phi_i^n\|^2+\|\nabla(2\phi_i^{n+1}-\phi_i^n)\|^2-\|\nabla(2\phi_i^n-\phi_i^{n-1})\|^2)\Big)\\ &+\frac{12}{\epsilon}\Big(|U^{n+1}|^2-|U^n|^2+|2U^{n+1}-U^n|^2-|2U^n-U^{n-1}|^2\Big)\\ &+\frac{1}{2}\Big(|Q^{n+1}|^2-|Q^n|^2+|2Q^{n+1}-Q^n|^2-|2Q^n-Q^{n-1}|^2\Big)\\ &+\frac{S}{\epsilon}\sum_{i=1}^{3}\Big(\Sigma_i\left(\|\phi_i^{n+1}-\phi_i^n\|^2-\|\phi_i^n-\phi_i^{n-1}\|^2\right)\Big)\\ &+\Big\{\frac{1}{2}\|\mathbf{u}^{n+1}-2\mathbf{u}^n+\mathbf{u}^{n-1}\|^2+\frac{3}{2}\|\mathbf{u}^{n+1}-\tilde{\mathbf{u}}^{n+1}\|^2\\ &\quad+\frac{3\epsilon}{8}\sum_{i=1}^{3}\Sigma_i\|\nabla(\phi_i^{n+1}-2\phi_i^n+\phi_i^{n-1})\|^2+\frac{12}{\epsilon}|U^{n+1}-2U^n+U^{n-1}|^2\\ &\quad+\frac{1}{2}|Q^{n+1}-2Q^n+Q^{n-1}|^2+\frac{2S}{\epsilon}\sum_{i=1}^{3}\Sigma_i\|\phi_i^{n+1}-2\phi_i^n+\phi_i^{n-1}\|^2\Big\}\\ &=-2\delta t\nu\|\nabla\tilde{\mathbf{u}}^{n+1}\|^2-2\delta tM\sum_{i=1}^{3}\Sigma_i\left\|\frac{\nabla\mu_i^{n+1}}{\Sigma_i}\right\|^2\\ &\le-2\delta t\nu\|\nabla\tilde{\mathbf{u}}^{n+1}\|^2-2\delta tM\underline{\Sigma}\sum_{i=1}^{3}\left\|\frac{\nabla\mu_i^{n+1}}{\Sigma_i}\right\|^2\le 0,\end{aligned}\tag{3.88}$$

where we use the following two identities

$$(3a-4b+c)(a-2b+c)=(a-b)^2-(b-c)^2+2(a-2b+c)^2,$$

and

$$\sum_{i=1}^{3}U^{n+1}\int_\Omega\beta^*(3\phi_i^{n+1}-4\phi_i^n+\phi_i^{n-1})d\boldsymbol{x}=U^{n+1}\int_\Omega\beta^*(\sum_{i=1}^{3}(3\phi_i^{n+1}-4\phi_i^n+\phi_i^{n-1}))d\boldsymbol{x}=0$$

which is due to (3.33).

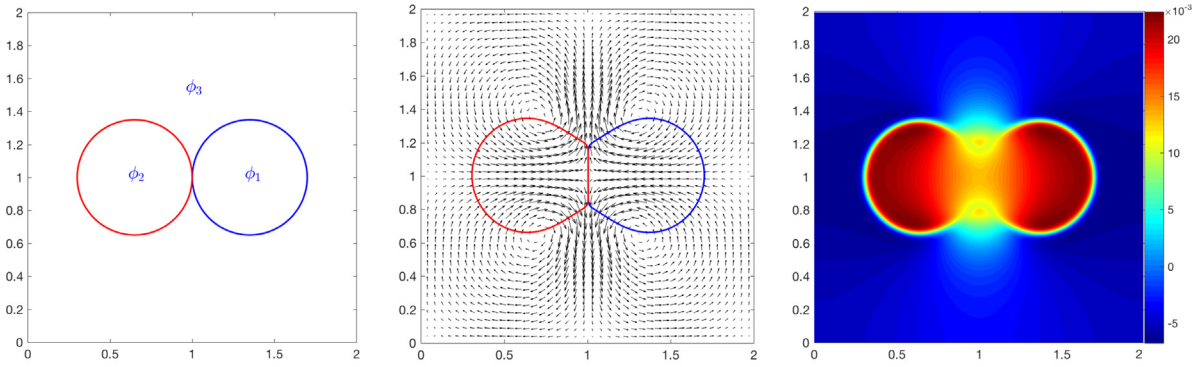

Fig. 4.1. (a) Initial interface contour of the three phase-field variables, (b) interface contour superimposed by the velocity field at the steady-state, and (c) the color plot of the pressure p at the steady-state. (For interpretation of the references to color in this figure legend, the reader is referred to the web version of this article.)

Finally, we obtain $E^{n+1} \geq 0$ by using (2.9) and (3.33). Likewise, we obtain (3.73) after dropping the terms in { } of (3.88) since they are positive, i.e.,

$$\begin{aligned} &\sum_{i=1}^{3} \Sigma_i \|\nabla(\phi_i^{n+1} - 2\phi_i^n + \phi_i^{n-1})\|^2 \geq \underline{\Sigma} \sum_{i=1}^{3} \|\nabla(\phi_i^{n+1} - 2\phi_i^n + \phi_i^{n-1})\|^2 \geq 0, \\ &\sum_{i=1}^{3} \Sigma_i \|\phi_i^{n+1} - 2\phi_i^n + \phi_i^{n-1}\|^2 \geq \underline{\Sigma} \sum_{i=1}^{3} \|\phi_i^{n+1} - 2\phi_i^n + \phi_i^{n-1}\|^2 \geq 0. \quad \square \end{aligned} \tag{3.89}$$

4. Numerical simulation

In this section, we use the proposed algorithm (3.20)–(3.26) to perform numerical simulations, including stability/accuracy tests, 2D spinodal decomposition, 2D contact lens deposited between two stratified fluids, as well as liquid droplet rising examples in 2D and 3D. In all numerical examples, we use the rectangular computational domain. For directions with periodic boundary conditions, the Fourier-spectral method is used for discretization. For directions with boundary conditions specified in (3.28), the Legendre–Galerkin method is adopted for discretization where the inf–sup stable pair (P_N, P_{N-2}) is used for the velocity ($\tilde{\mathbf{u}}$ and $\mathbf{u}$) and pressure p, respectively, and P_N is used for the phase-field variables ϕ_1, ϕ_2, ϕ_3.

4.1. Stability and accuracy test

We first perform several stability tests in 2D to verify the unconditional energy stability of the fully-decoupled scheme (3.20)–(3.26). We set the 2D computational domain to be $[0, 2]^2$. The initial conditions for all variables are given by

$$\begin{cases} \phi_i^0(x, y, t = 0) = \tanh(\dfrac{r - \sqrt{(x - x_i)^2 + (y - y_i)^2}}{\epsilon}), \, i = 1, 2, \\ \phi_3^0 = 1 - \phi_1^0 - \phi_2^0, \, \mathbf{u}^0 = (u^0, v^0) = (0, 0), \, p^0 = 0, \end{cases} \tag{4.1}$$

where $\epsilon = 0.05$, $r = 0.35$, $x_1 = 1.35$, $x_2 = 0.65$, and $y_1 = y_2 = 1$. The order parameters are set as

$$M = 1\text{e}{-3}, \, \Lambda = 7, \, B = 10, \, (\sigma_{12}, \sigma_{13}, \sigma_{23}) = 0.01(1, 1, 1), \, S = 4. \tag{4.2}$$

The initial interface contours $\{\phi_i^0 = \frac{1}{2}\}$ of the three phase-field variables are shown in Fig. 4.1(a). We assume that the boundary conditions are periodic and space is discretized by using the Fourier-spectral method where 257 Fourier modes are used to discretize each direction.

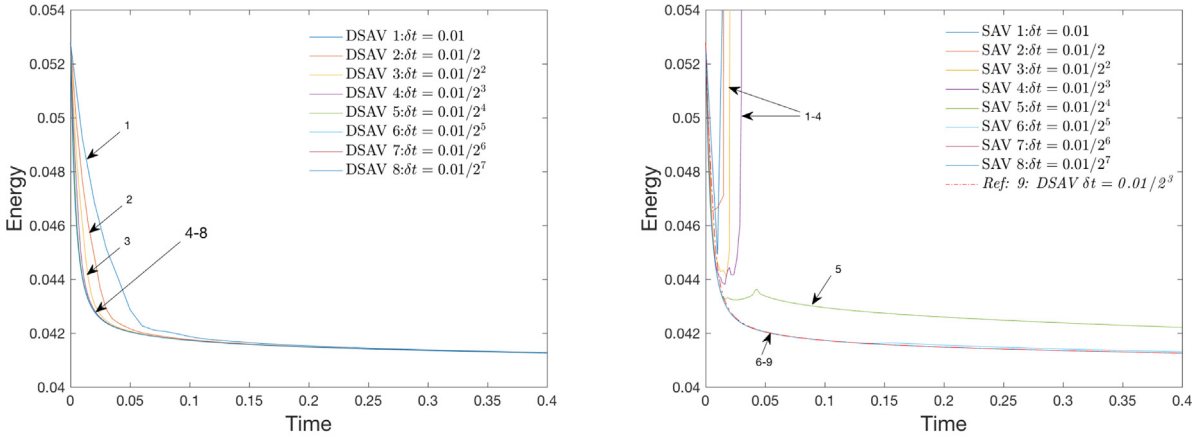

(a) DSAV. (b) SAV.

Fig. 4.2. The time evolution of the total free energy (3.74) computed by using the scheme DSAV and SAV with different time steps, where the initial conditions are given by (4.1) and model parameters are given by (4.2).

Using the above initial conditions and a time step of $\delta t = \frac{0.01}{2^3}$, we implement the algorithm until a steady-state solution is obtained, and plot the fluid interface with the velocity field at the steady-state in Fig. 4.1(b). We can see that due to the balanced surface tension coefficients of the three fluid components and coarsening effects, the two droplets squeeze together to form a contact angle of 120°. In Fig. 4.1(c), we plot the profile of the pressure p at the steady-state using a color diagram.

Next, we verify whether the scheme maintains energy stability unconditionally using any time step. For convenience, we represent the developed decoupled scheme (3.20)–(3.26) using scalar auxiliary variables by DSAV. Meanwhile, in order to illustrate the advantages of the developed decoupling technique and the added stabilizer in improving energy stability, we also test the stability of the scheme DSAV, but the variable Q^{n+1} and S are removed (i.e., assume $Q^{n+1} \equiv 1$ and $S = 0$). For convenience, we refer to this version as SAV.

In Fig. 4.2(a), we plot the evolution curves of the total free energy (3.74) calculated by the scheme DSAV using different time steps. We find that all calculated energy curves show monotonic attenuation, which confirms the unconditional stability of DSAV. When the time step is relatively large, the energy curve with a large time step has an observable deviation from the energy curve with a small time step. This is because the errors obtained using large time steps are also large. When the time step is less than $\frac{0.01}{2^3}$, the five energy curves obtained are very close, which is why we use the time step size $\frac{0.01}{2^3}$ to obtain the equilibrium solution shown in Fig. 4.1. For comparison, in Fig. 4.2(b), we plot the energy evolution curves calculated by SAV, and observe that it blows up while a large time step size is used, and only decays when $\delta t \leq \frac{0.01}{2^5}$.

Through performing mesh refinement tests in time for the example above, we further test the convergence order of the developed scheme DSAV. Since the exact solutions are unknown, the numerical solution obtained by the scheme DSAV using a very small time step ($\delta t = 1\text{e}{-9}$) is regarded as an exact solution for calculating the approximate error. Then, we plot the L^2 errors of all variables at $t = 0.4$ obtained by changing the time step size from 0.01 to $\frac{0.01}{2^7}$ with a factor of $1/2$. The convergence rate is shown in Fig. 4.3(a), where we find that the scheme DSAV always exhibits almost perfect second-order accuracy. In Fig. 4.3(b), we compare the accuracy of DSAV and SAV by plotting the arithmetic mean of L^2 numerical errors of the three phase-field variables. When the time step size is large ($\delta t > \frac{0.01}{2^6}$), SAV completely loses the convergence order. When the time step size is small ($\delta t \leq \frac{0.01}{2^6}$), it has the second-order accuracy. For comparison, DSAV consistently shows good second-order accuracy in all tested time steps. If we compare the size of the error when $\delta t \leq \frac{0.01}{2^6}$, we find that the error obtained by SAV is smaller than that obtained by DSAV. This is because the stabilization terms increase some splitting errors.

4.2. Spinodal decomposition

In this example, we study the equilibrium pattern obtained after phase separation (or spinodal decomposition). The initial conditions are set as a homogeneous ternary mixture but with some small perturbations, which read as

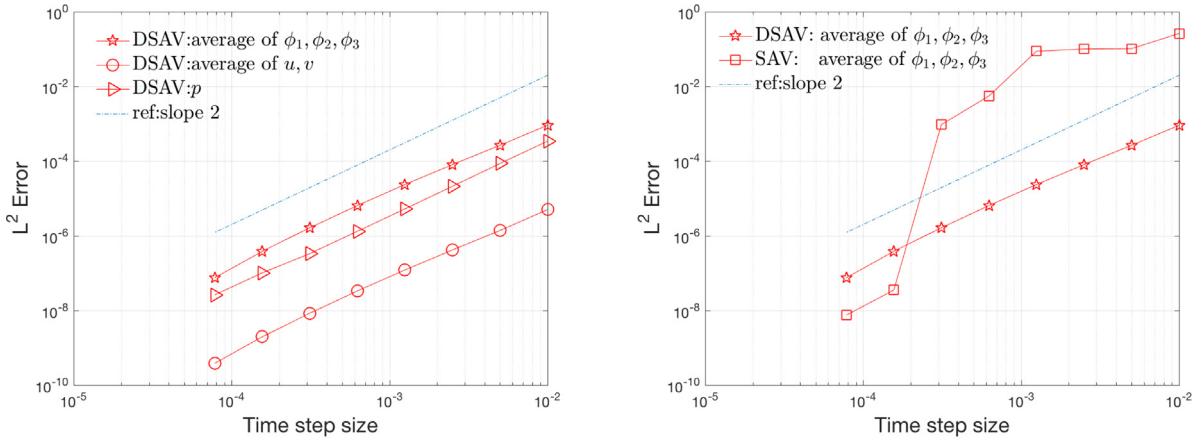

(a) All variables of DSAV. (b) DSAV and SAV.

Fig. 4.3. The numerical errors in L^2 of all variables that are computed using the schemes DSAV and SAV with various temporal resolutions.

follows,

$$\mathbf{u}^0(\boldsymbol{x}) = \mathbf{0},\ p^0(\boldsymbol{x}) = 0,\ \phi_i^0(\boldsymbol{x}) = \frac{\psi_i}{\psi_1 + \psi_2 + \psi_3},\ i = 1, 2, 3, \tag{4.3}$$

where $\psi_i(\boldsymbol{x}) = 0.5 + 0.001\text{rand}(\boldsymbol{x})$ and $\text{rand}(\boldsymbol{x})$ is the random number in $[-1, 1]$ that follows the normal distribution.

We use the 2D computational domain $[0, 2]^2$ and adopt periodic boundary conditions. The space is discretized by using the Fourier-spectral methods with 257 Fourier modes for each direction. The model parameters are set to

$$M = 1\text{e}{-2},\ \nu = 1,\ \Lambda = 7,\ B = 10,\ \epsilon = 0.02,\ S = 4. \tag{4.4}$$

We adjust the surface tension $(\sigma_{12}, \sigma_{13}, \sigma_{23})$ to study how the three phases are separated.

We first perform simulations for two partial spreading cases with $(\sigma_{12}, \sigma_{13}, \sigma_{23}) = 0.1(1, 1, 1)$ and $0.1(1, 0.8, 1.4)$. Snapshots of the profiles $\frac{1}{2}\phi_1 + \phi_2$ at various times up to the steady-state are shown in Fig. 4.4(a) and (b). For the case with three equal surface tension parameters, shown in Fig. 4.4(a), the final equilibrium solution is a hexagonal pattern, and three contact angles all become $\frac{2\pi}{3}$. For the latter case, we find that the steady-state solution exhibits different contact angles. The total spreading case with $(\sigma_{12}, \sigma_{13}, \sigma_{23}) = 0.1(3, 1, 1)$ is shown in Fig. 4.4(c) and no junction points are observed. In Fig. 4.5, we plot the time evolution of the logarithm of the free energy functional (3.74) for all simulations in which all energy curves show the decay over time, thus confirming the developed algorithm is unconditionally stable.

4.3. Liquid lens between two stratified fluids

In this example, we simulate the steady-state solutions of a liquid lens with different surface tension coefficients. The initial condition is set to a circular lens, which is located at the interface between the other two stratified immiscible fluids, see [2–4,6,7]. The 2D computed domain is set as $(x, y) \in \Omega = [0, 1] \times [0, 0.5]$ and the initial conditions read as follows,

$$\begin{cases} \mathbf{u}^0(x, y) = \mathbf{0},\ p^0(x, y) = 0, \\ \phi_1^0(x, y) = (1 - \phi_3^0)\left(\frac{1}{2} + \frac{1}{2}\tanh\left(\frac{4}{\epsilon}(y - 0.25)\right)\right) \\ \phi_2^0(x, y) = 1 - \phi_1^0 - \phi_3^0, \\ \phi_3^0(x, y) = \frac{1}{2}\tanh\left(\frac{0.09 - \sqrt{(x - 0.5)^2 + (y - 0.25)^2}}{\epsilon/2}\right) + \frac{1}{2}. \end{cases} \tag{4.5}$$

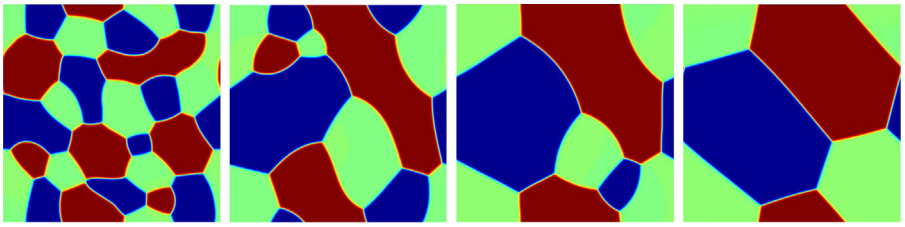

(a) Snapshots taken at $t = 1,\ 5,\ 10,\ 20$ with $(\sigma_{12}, \sigma_{13}, \sigma_{23})$=$0.1(1, 1, 1)$.

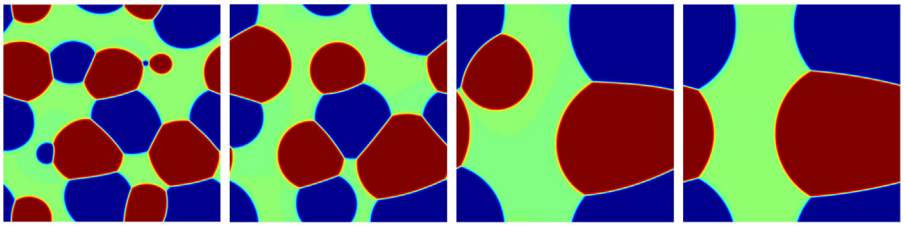

(b) Snapshots taken at $t = 1,\ 5,\ 20,\ 50$ with $(\sigma_{12}, \sigma_{13}, \sigma_{23})$=$0.1(1, 0.8, 1.4)$.

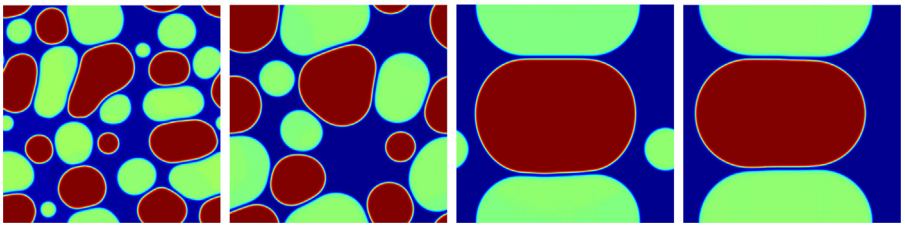

(c) Snapshots taken at $t = 1,\ 5,\ 50,\ 70$ with $(\sigma_{12}, \sigma_{13}, \sigma_{23})$=$0.1(3, 1, 1)$.

Fig. 4.4. Dynamical evolution of the profile $\frac{1}{2}\phi_1+\phi_2$ for the spinodal decomposition examples with three different surface tension parameters.

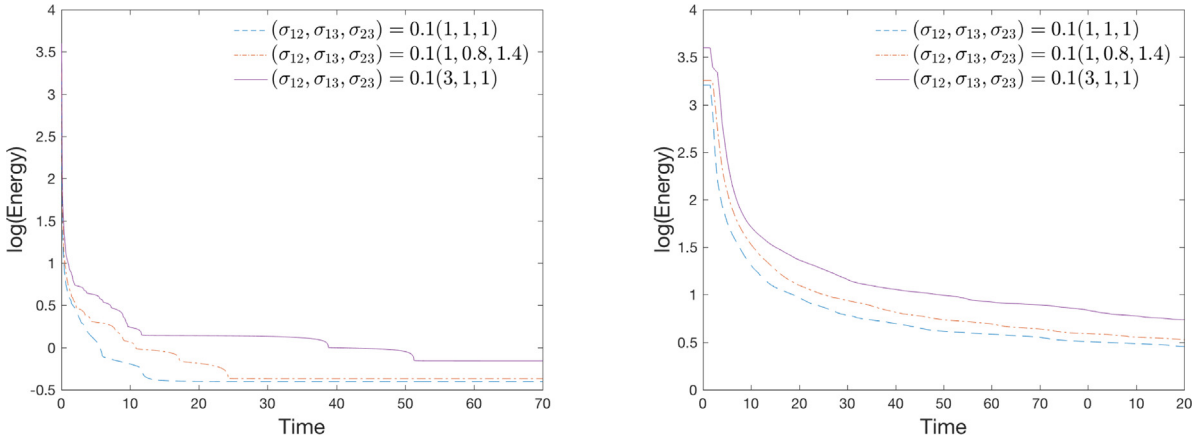

(a) Energy evolution over time. (b) A close-up view for $t \in (0, 20)$.

Fig. 4.5. Time evolution of the logarithm of the total free energy (3.74) of all spinodal decomposition examples.

We assume that the x-direction follows the periodic boundary conditions and use the Fourier-spectral method with 257 Fourier modes to discretize it. For the y-direction, we set the boundary conditions of the variables $\mathbf{u} = (u, v)$, ϕ_i and μ_i to

$$u|_{(y=0,0.5)} = 0,\ \ v|_{(y=0,0.5)} = \partial_{\mathbf{n}}\phi_i|_{(y=0,0.5)} = \partial_{\mathbf{n}}\mu_i|_{(y=0,0.5)} = 0. \tag{4.6}$$

Table 4.1
Surface tension parameters $(\sigma_{12}, \sigma_{13}, \sigma_{23})$ and the theoretical prediction of contact angles $\theta_1, \theta_2, \theta_3$ derived from (4.8).

$(\sigma_{12}, \sigma_{13}, \sigma_{23})$	(1,1,1)	(1,1,0.6)	(1,0.6,0.6)	(1,0.8,1.4)
(partial spreading)	$\theta_1 = \theta_2 = \theta_3$	$\theta_1 > \theta_2 = \theta_3$	$\theta_1 = \theta_2 > \theta_3$	$\theta_1 < \theta_3 < \theta_2$
$(\sigma_{12}, \sigma_{13}, \sigma_{23})$	(1,1,3)		(3,1,1)	
(total spreading)	$\theta_1 = 0, \theta_2 = \theta_3 = \pi$		$\theta_1 = \theta_2 = \pi, \theta_3 = 0$	

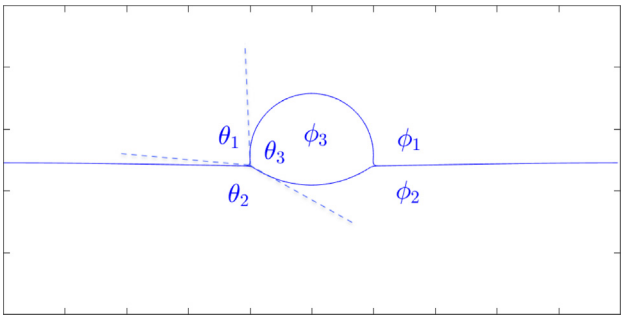

Fig. 4.6. The schematic diagram of contact lens and contact angles.

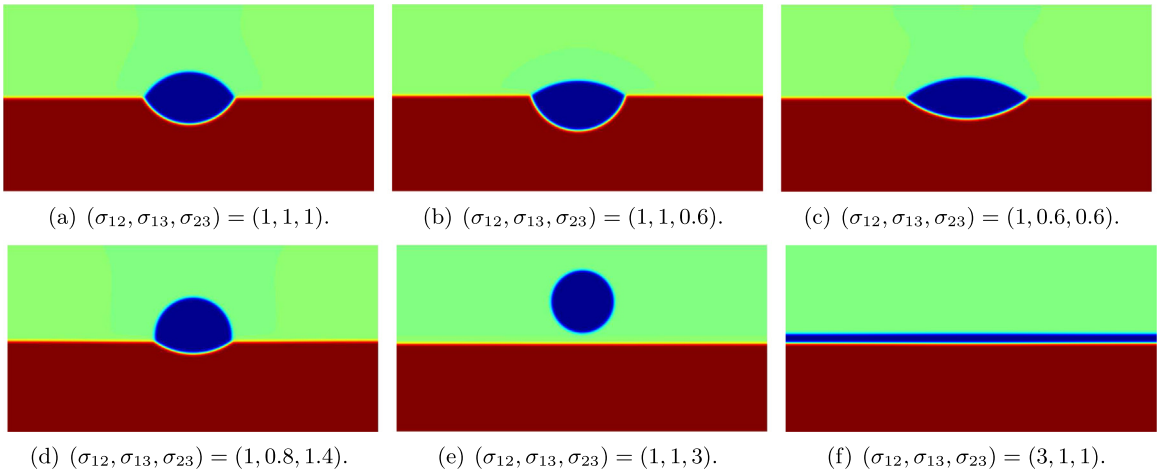

(a) $(\sigma_{12}, \sigma_{13}, \sigma_{23}) = (1, 1, 1)$. (b) $(\sigma_{12}, \sigma_{13}, \sigma_{23}) = (1, 1, 0.6)$. (c) $(\sigma_{12}, \sigma_{13}, \sigma_{23}) = (1, 0.6, 0.6)$.

(d) $(\sigma_{12}, \sigma_{13}, \sigma_{23}) = (1, 0.8, 1.4)$. (e) $(\sigma_{12}, \sigma_{13}, \sigma_{23}) = (1, 1, 3)$. (f) $(\sigma_{12}, \sigma_{13}, \sigma_{23}) = (3, 1, 1)$.

Fig. 4.7. The steady-state solutions of the contact lens with various surface tension parameters computed by the scheme DSAV.

Then the y-direction is discretized using the Legendre–Galerkin spectral method with the Legendre polynomials up to the degree of 512. We set the model parameters to

$$M = 1\text{e}{-5}, \Lambda = 7, B = 10, \epsilon = 0.01, S = 4, \delta t = 1\text{e}{-3}. \tag{4.7}$$

In the limit $\epsilon \to 0$, the relationship between the contact angles of the equilibrium state (the schematic diagram of the contact angles and three fluid components is shown in Fig. 4.6) and three surface tension parameters are given by the Young's relationship (cf. [1,2,45]),

$$\frac{\sin\theta_1}{\sigma_{23}} = \frac{\sin\theta_2}{\sigma_{13}} = \frac{\sin\theta_3}{\sigma_{12}}. \tag{4.8}$$

Therefore, we adjust the three surface tension parameters $(\sigma_{12}, \sigma_{13}, \sigma_{23})$ to investigate whether the contact angles under steady-state follows the theoretical predictions from (4.8).

We use four partial spreading cases and two total spreading cases in the computations. Theoretical prediction values of the contact angles according to the given surface tension parameters are shown in Table 4.1. In Fig. 4.7,

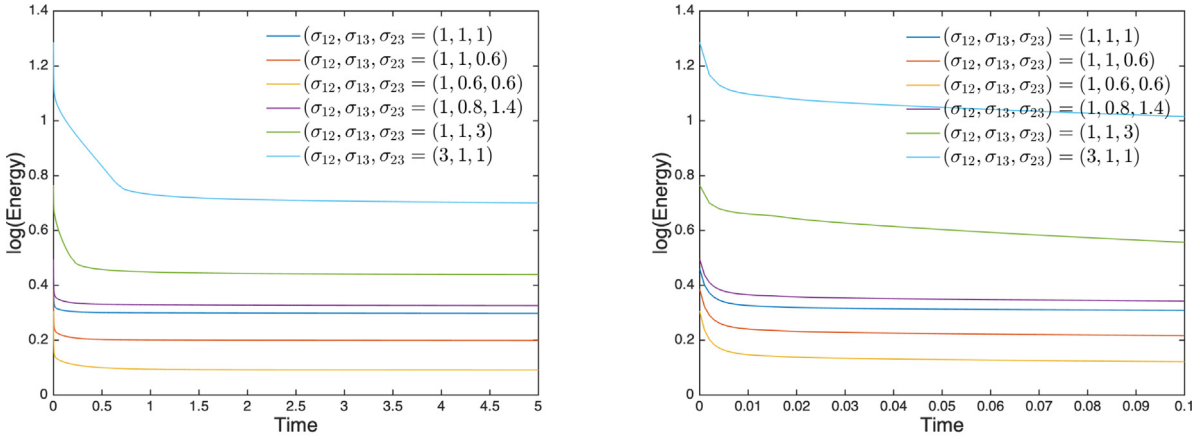

(a) Energy evolution over time. (b) A close-up view for $t \in (0, 20)$.

Fig. 4.8. Time evolution of the logarithm of the total free energy (3.74) of all contact lens examples.

using the scheme DSAV, for each case, we plot the steady-state solution for the profile of $\frac{1}{2}\phi_1 + \phi_2$. We can see that the calculation can well verify the theoretical prediction of the contact angle. In addition, all these calculations are consistent in quality with the numerical simulations provided in [2,4–7]. In Fig. 4.8, we plot the time evolution of the total free energy in all simulated cases.

4.4. The dynamics of a rising liquid droplet

In this example, we study how a light liquid droplet rises and deforms as it passes through the liquid/liquid interface under the influence of gravity and surface tensions. For simplicity, we consider the situation that the density difference between the liquid droplet and the other two ambient fluids is small, so we can use the Boussinesq approximation (see also in [42,46,47]) and replace the momentum equation as follows:

$$\mathbf{u}_t + \mathbf{u}\cdot\nabla\mathbf{u} - \nu\Delta\mathbf{u} + \nabla p + \sum_{i=1}^{3}\phi_i\nabla\mu_i = \mathbf{g}_0\phi_3, \tag{4.9}$$

where $\mathbf{g}_0 = (0, g_0)$ for 2D, $\mathbf{g}_0 = (0, 0, g_0)$ for 3D, and g_0 is the pre-assumed gravity constant.

First, we perform several simulations in 2D, where the computational domain is set to $(x, y) \in \Omega = [0, 2]\times[0, 4]$. Periodic boundary conditions are set for the x-direction, and we discretize it using the 257 Fourier modes. For the y-direction, we use the boundary conditions specified in (3.28), and use the Legendre polynomials with the degree up to 512 for discretization. The initial conditions for variables ϕ_i (the schematic diagram of the three fluid components are shown in Fig. 4.9(a)), $\mathbf{u}$, and p are set as follows,

$$\begin{aligned}
&\phi_1^0(x, y) = (1-\phi_3^0)\left(\frac{1}{2} + \frac{1}{2}\tanh\Big(\frac{4}{\epsilon}(y-2)\Big)\right),\\
&\phi_2^0(x, y) = 1 - \phi_1^0 - \phi_3^0,\\
&\phi_3^0(x, y) = \frac{1}{2}\tanh\Big(\frac{0.25 - \sqrt{(x-1)^2 + (y-1)^2}}{\epsilon/2}\Big) + \frac{1}{2},\\
&\mathbf{u}^0(x, y) = (0, 0),\ p^0(x, y) = 0.
\end{aligned} \tag{4.10}$$

The model parameters read as

$$M = 1\text{e}{-4},\ \nu = 1,\ \Lambda = 7,\ B = 10,\ \epsilon = 0.05,\ S = 4,\ \delta t = 1\text{e}{-3}. \tag{4.11}$$

We vary the surface tension parameters $(\sigma_{12}, \sigma_{13}, \sigma_{23})$ and the gravity parameter g_0 to study how the droplet rises and deforms with time.

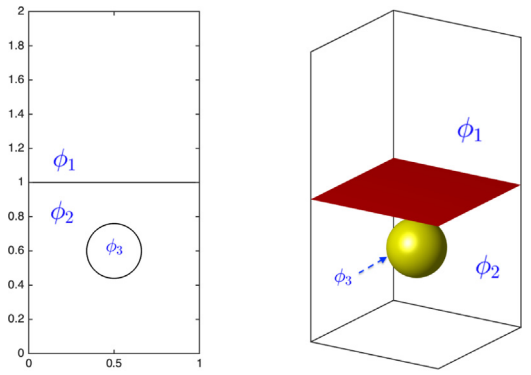

(a) 2D. (b) 3D.

Fig. 4.9. Initial schematic diagram of a rising liquid droplet example in 2D and 3D.

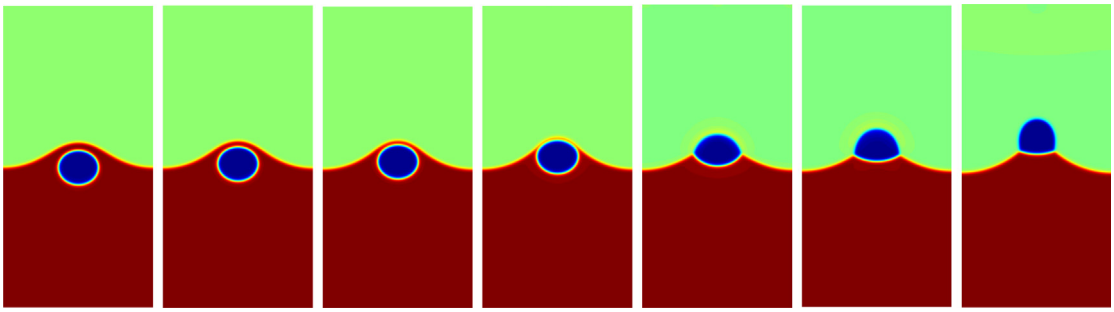

Fig. 4.10. The dynamics of a 2D rising liquid droplet with $(\sigma_{12}, \sigma_{13}, \sigma_{23}) = 10(1, 1, 1)$ and gravity parameters $g_0 = 90$. Snapshots of the profile $\frac{1}{2}\phi_1 + \phi_2$ are taken at $t = 1, 1.2, 1.4, 1.6, 1.8, 2$ and 14.

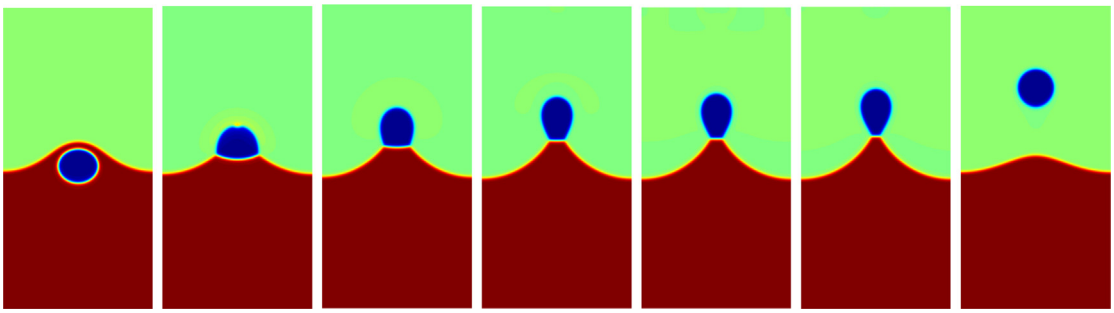

Fig. 4.11. The dynamics of a 2D rising liquid droplet with $(\sigma_{12}, \sigma_{13}, \sigma_{23}) = 10(1, 1, 1)$ and gravity parameter $g_0 = 100$. Snapshots of the profile $\frac{1}{2}\phi_1 + \phi_2$ are taken at $t = 1, 2, 4, 7, 8, 9$, and 10.

We first set the three surface tension parameters to $(\sigma_{12}, \sigma_{13}, \sigma_{23}) = 10(1, 1, 1)$ and use two different gravity parameters $g_0 = 90$ and 100. Figs. 4.10 and 4.11 shown numerical solutions at various times, of which snapshots of the profiles of $\frac{1}{2}\phi_1 + \phi_2$ are plotted. When the gravity constant is relatively weak ($g_0 = 90$), we find that the droplet is captured by the interface of the two layered fluids. When the gravity constant is large ($g_0 = 100$), the droplet passes through the interface and enters the upper fluid.

Furthermore, we change the surface tension parameter to $(\sigma_{12}, \sigma_{13}, \sigma_{23}) = 10(1, 0.6, 0.6)$, and also use two different gravity parameters $g_0 = 90$ and 100, shown in Figs. 4.12 and 4.13. Similar to the previous two simulations, similar phenomena are observed, including the low gravity parameter leading to capture and high gravity parameter leading to interface penetration. In addition, when $g_0 = 90$, we see that the contact angle caused by the suspension

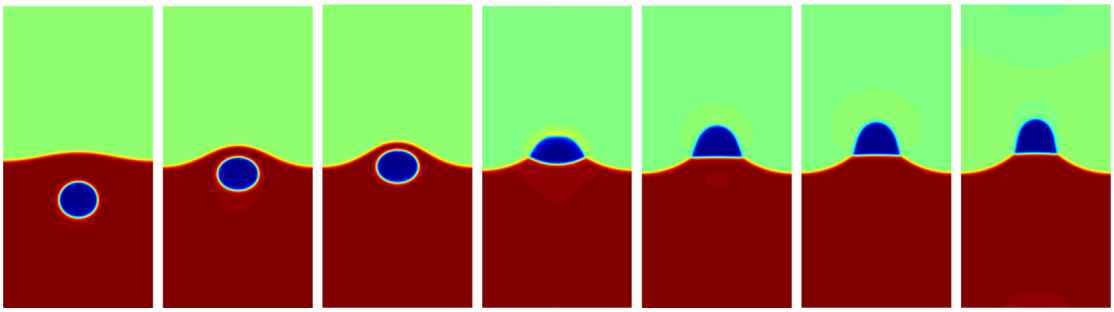

Fig. 4.12. The dynamics of a 2D rising liquid droplet with $(\sigma_{12}, \sigma_{13}, \sigma_{23}) = 10(1, 0.6, 0.6)$ and gravity parameter $g_0 = 90$. Snapshots of the profile $\frac{1}{2}\phi_1 + \phi_2$ are taken at $t = 0.4, 0.8, 1, 1.8, 3, 4,$ and 15.

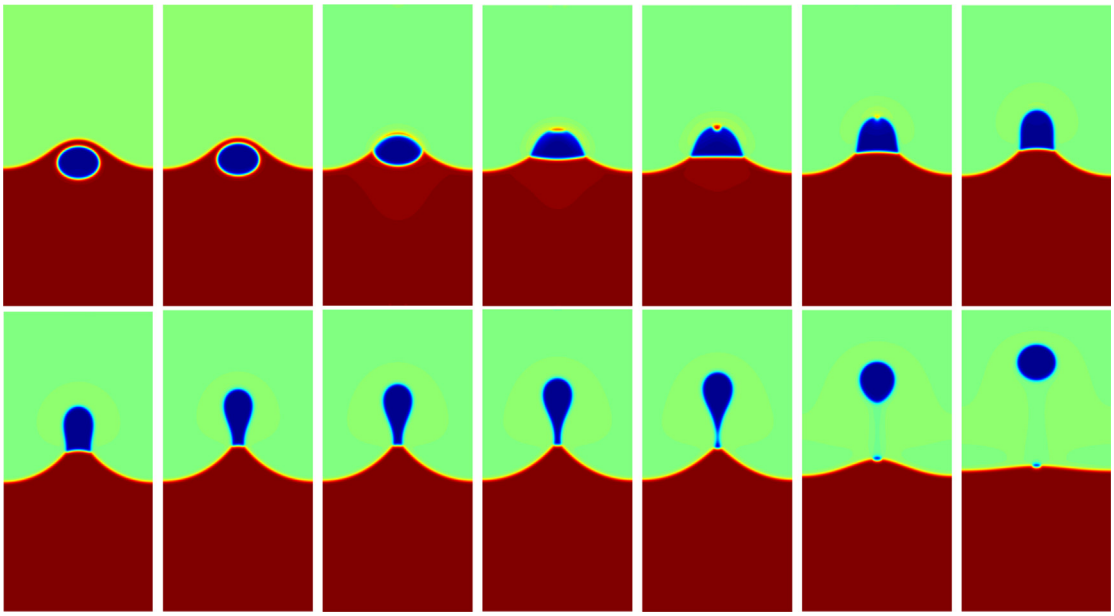

Fig. 4.13. The dynamics of a 2D rising liquid droplet with $(\sigma_{12}, \sigma_{13}, \sigma_{23}) = 10(1, 0.6, 0.6)$ and gravity parameter $g_0 = 100$. Snapshots of the profile $\frac{1}{2}\phi_1 + \phi_2$ are taken at $t = 1, 1.2, 1.6, 1.8, 2, 3, 4, 5, 6, 6.2, 6.4, 6.6, 6.8,$ and 7.

of the droplet is different from the situation of $(\sigma_{12}, \sigma_{13}, \sigma_{23}) = 10(1, 1, 1)$. When $g_0 = 120$, we see that the liquid rupture twice, the first rupture occurs at $t = 1.6$, which is due to the rise of the droplet and squeezes the lower fluid, and the second occurs at $t = 6.6$ when the filament formed by the rising droplet breaks.

Finally, we perform 3D simulations by setting the computational domain is set as $\Omega = [0, 1] \times [0, 1] \times [0, 2]$. Similar to the 2D simulations, the periodic boundary conditions in the x and y-directions are assumed, and 129 Fourier modes are adopted to discretize each direction. The z-direction follows the boundary conditions given in (3.28), which is discretized by using Legendre polynomials up to the degree of 256. The initial conditions are set as follows,

$$\begin{cases} \phi_1^0(x, y, z) = (1 - \phi_3^0)\left(\dfrac{1}{2} + \dfrac{1}{2}\tanh\left(\dfrac{5.5}{\epsilon}(z - 1)\right)\right), \\ \phi_2^0(x, y, z) = 1 - \phi_1^0 - \phi_3^0, \\ \phi_3^0(x, y, z) = \dfrac{1}{2}\tanh\left(\dfrac{0.25 - \sqrt{(x - 0.5)^2 + (y - 0.5)^2 + (z - 0.6)^2}}{\epsilon/2}\right) + \dfrac{1}{2}, \\ \mathbf{u}^0(x, y, z) = (0, 0, 0),\ p^0(x, y, z) = 0. \end{cases} \tag{4.12}$$

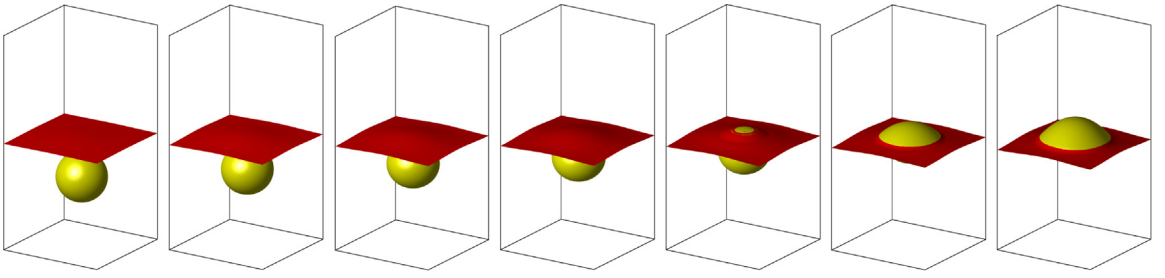

(a) $(\sigma_{12}, \sigma_{13}, \sigma_{23}) = 2(1, 0.6, 0.6)$, $g_0 = 40$. Snapshots are taken at $t = 0.2, 0.6, 1, 1.4, 1.8, 2.2$, and 8.2.

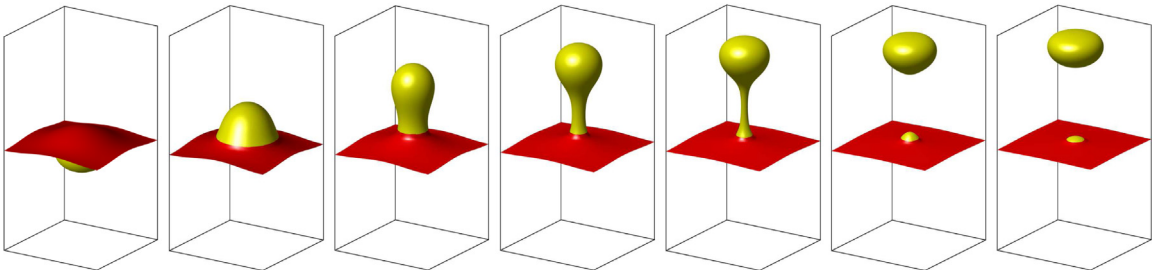

(b) $(\sigma_{12}, \sigma_{13}, \sigma_{23}) = 2(1, 0.6, 0.6)$, $g_0 = 50$. Snapshots are taken at $t = 1, 2.2, 4.2, 5, 5.4, 5.8$, and 6.2.

Fig. 4.14. The dynamics of a 3D rising liquid droplet with $(\sigma_{12}, \sigma_{13}, \sigma_{23}) = 2(1, 0.6, 0.6)$ and gravity parameter (a) $g_0 = 40$ and (b) $g_0 = 50$. Snapshots of the isosurfaces $\{\phi_3 = 0.5\}$ (yellow) and $\{\phi_1 = 0.5\}$ (red) are plotted in each subfigure. (For interpretation of the references to color in this figure legend, the reader is referred to the web version of this article.)

The initial condition for these three fluid components are outlined in Fig. 4.9(b). The model parameters read as

$$M = 1\text{e}{-4}, \nu = 1, \Lambda = 7, B = 10, \epsilon = 0.05, S = 4, \delta t = 1\text{e}{-3}. \tag{4.13}$$

In Fig. 4.14(a) and (b), we adopt the surface tension parameter $(\sigma_{12}, \sigma_{13}, \sigma_{23}) = 2(1, 0.6, 0.6)$ and different gravity parameters $g_0 = 40$ and $g_0 = 50$, respectively. We use different colors to plot the isosurfaces of $\{\phi_1 = 0.5\}$ (yellow) and $\{\phi_3 = 0.5\}$ (red). Similar to the 2D simulation, lower gravity causes the droplet to be captured by the interface, while higher gravity cause the droplet to penetrate the interface. In addition to the capture/penetration phenomenon, we also find that when the gravity constant is large, a long filament forms after the droplet penetrates the interface, and then the rupture of the filament occurs (at $t = 5.4$).

5. Concluding remarks

In this paper, with the help of two nonlocal auxiliary variables, a novel second-order fully-decoupled numerical algorithm is developed to solve the highly nonlinear phase-field model of three-phase incompressible flow. The scheme only needs to solve several decoupled linear elliptic equations with constant coefficients at each time step to obtain a numerical solution with second-order time accuracy. Solvability and unconditional energy stability have also been rigorously proven, and a large number of numerical simulations have been performed in 2D and 3D to show the accuracy and stability of the scheme numerically. Moreover, the novel decoupling method proposed in this paper can be widely applied to a large number of coupling models, as long as the nonlinear coupling terms satisfy the so-called "*zero-energy-contribution*" characteristic.

Declaration of competing interest

The authors declare that they have no known competing financial interests or personal relationships that could have appeared to influence the work reported in this paper.

Acknowledgments

X. Yang was partially supported by National Science Foundation, USA with grant numbers DMS-1720212, DMS-1818783 and DMS-2012490.

References

[1] J. Kim, J. Lowengrub, Phase field modeling and simulation of three-phase flows, Interfaces Free Bound. 7 (2005) 435–466.
[2] F. Boyer, S. Minjeaud, Numerical schemes for a three component Cahn–Hilliard model, ESAIM Math. Model. Numer. Anal. 45 (04) (2011) 697–738.
[3] F. Boyer, C. Lapuerta, S. Minjeaud, B. Piar, M. Quintard, Cahn–Hilliard/navier-stokes model for the simulation of three-phase flows, Transp. Porous Media 82 (2010) 463–483.
[4] F. Boyer, C. Lapuerta, Study of a three component Cahn–Hilliard flow model, ESAIM Math. Model. Numer. Anal. 40 (4) (2006) 653–687.
[5] X. Yang, J. Zhao, Q. Wang, J. Shen, Numerical approximations for a three components Cahn-Hilliard phase-field model based on the invariant energy quadratization method, M3AS Math. Models Methods Appl. Sci. 27 (2017) 1993–2030.
[6] J. Zhang, X. Yang, Decoupled, non-iterative, and unconditionally energy stable large time stepping method for the three-phase Cahn-Hilliard phase-field model, J. Comput. Phys. 404 (2020) 109115.
[7] J. Zhang, X. Yang, Unconditionally energy stable large time stepping method for the L2-gradient flow based ternary phase-field model with precise nonlocal volume conservation, Comput. Methods Appl. Mech. Engrg. 361 (2020) 112743.
[8] S. Minjeaud, An unconditionally stable uncoupled scheme for a triphasic Cahn–Hilliard/Navier–Stokes model, Numer. Methods Partial Differential Equations 29 (2) (2013) 584–618.
[9] J. Shen, X. Yang, Numerical approximations of Allen–Cahn and Cahn–Hilliard equations, Discrete Contin. Dyn. Syst. A 28 (2010) 1669–1691.
[10] Y. Cai, H. Choi, J. Shen, Error estimates for time discretizations of Cahn-Hilliard and Allen-Cahn phase-field models for two-phase incompressible flows, Numer. Math. 137 (2017) 417–449.
[11] H. Yu, X. Yang, Decoupled energy stable schemes for phase field model with contact lines and variable densities, J. Comput. Phys. 334 (2017) 665–686.
[12] J. Shen, X. Yang, Decoupled, energy stable schemes for phase-field models of two-phase incompressible flows, SIAM J. Numer. Anal. 53 (1) (2015) 279–296.
[13] J. Shen, C. Wang, S. Wang, X. Wang, Second-order convex splitting schemes for gradient flows with ehrlich-schwoebel type energy: application to thin film epitaxy, SIAM J. Numer. Anal. 50 (2012) 105–125.
[14] D.J. Eyre, Unconditionally gradient stable time marching the Cahn-Hilliard equation, in: Computational and Mathematical Models of Microstructural Evolution (San Francisco, CA, 1998), in: Mater. Res. Soc. Sympos. Proc., vol. 529, MRS, 1998, pp. 39–46.
[15] S.M. Wise, C. Wang, J.S. Lowengrub, An energy-stable and convergent finite-difference scheme for the phase field crystal equation, SIAM J. Numer. Anal. 47 (3) (2009) 2269–2288.
[16] Z. Hu, S.M. Wise, C. Wang, J.S. Lowengrub, Stable and efficient finite difference nonlinear-multigrid schemes for the phase field crystal equation, J. Comput. Phys. 228 (2009) 5323–5339.
[17] D. Han, X. Wang, A second order in time, uniquely solvable, unconditionally stable numerical scheme for Cahn–Hilliard–Navier–Stokes equation, J. Comput. Phys. 290 (2015) 139–156.
[18] J. Shen, X. Yang, The IEQ and SAV approaches and their extensions for a class of highly nonlinear gradient flow systems, Contemp. Math. 754 (2020) 217–245.
[19] X. Yang, A novel fully-decoupled scheme with second-order time accuracy and unconditional energy stability for the Navier–Stokes equations coupled with mass-conserved Allen-Cahn phase-field model of two-phase incompressible flow, Internat. J. Numer. Methods Engrg. (2020) http://dx.doi.org/10.1002/nme.6578.
[20] X. Yang, H. Yu, Efficient second order unconditionally stable schemes for a phase field moving contact line model using an invariant energy quadratization approach, SIAM J. Sci. Comput. 40 (2018) B889–B914.
[21] X. Yang, Linear, first and second order and unconditionally energy stable numerical schemes for the phase field model of homopolymer blends, J. Comput. Phys. 327 (2016) 294–316.
[22] C. Chen, X. Yang, Efficient numerical scheme for a dendritic solidification phase field model with melt convection, J. Comput. Phys. 388 (2019) 41–62.
[23] X. Yang, Numerical approximations of the Navier–Stokes equation coupled with volume-conserved multi-phase-field vesicles system: fully-decoupled, linear, unconditionally energy stable and second-order time-accurate numerical scheme, Comput. Methods Appl. Mech. Engrg. 375 (2021) 113600.
[24] X. Yang, A novel fully-decoupled, second-order and energy stable numerical scheme of the conserved Allen-Cahn type flow-coupled binary surfactant model, Comput. Methods Appl. Mech. Engrg. 373 (2021) 113502.
[25] J. Shen, J. Xue, J. Yang, The scalar auxiliary variable (SAV) approach for gradient flows, J. Comput. Phys. 353 (2018) 407–416.
[26] C. Chen, X. Yang, Fast, provably unconditionally energy stable, and second-order accurate algorithms for the anisotropic Cahn-Hilliard model, Comput. Methods Appl. Mech. Engrg. 351 (2019) 35–59.
[27] Z. Yang, S. Dong, An unconditionally energy-stable scheme based on an implicit auxiliary energy variable for incompressible two-phase flows with different densities involving only precomputable coefficient matrices, J. Comput. Phys. 393 (2018) 229–257.
[28] Q. Du, R.A. Nicolaides, Numerical analysis of a continuum model of phase transition, SIAM J. Numer. Anal. 28 (1991) 1310–1322.
[29] H. Gomez, der Zee Van, G. Kristoffer, Computational phase-field modeling, in: Encyclopedia of Computational Mechanics, second ed., John Wiley & Sons, Ltd, ISBN: 978-1-119-00379-3, 2017.
[30] H. Gomez, V.M. Calo, Y. Bazilevs, T.J.R. Hughes, Isogeometric analystis of the cahn-hilliard phase-field model, Comput. Methods Appl. Mech. Engrg. 197 (2008) 4333–4352.
[31] I. Romero, Thermodynamically consistent time stepping algorithms for nonlinear thermomechanical systems, Internat. J. Numer. Methods Engrg. 79 (2009) 706–732.

[32] R. Nochetto, J.-H. Pyo, The gauge-Uzawa finite element method part I: the Navier-Stokes equations, SIAM J. Numer. Anal. 43 (2005) 1043–1068.
[33] J.L. Guermond, P. Minev, J. Shen, An overview of projection methods for incompressible flows, Comput. Methods Appl. Mech. Engrg. 195 (2006) 6011–6045.
[34] J.L. Guermond, L. Quartapelle, A projection FEM for variable density incompressible flows, J. Comput. Phys. 165 (1) (2000) 167–188.
[35] J. Shen, X. Yang, A phase-field model and its numerical approximation for two-phase incompressible flows with different densities and viscositites, SIAM J. Sci. Comput. 32 (2010) 1159–1179.
[36] W. Chen, W. Feng, Y. Liu, C. Wang, S. Wise, A second order energy stable scheme for the Cahn-Hilliard-Hele-Shaw equation, Discrete Contin. Dyn. Syst. Ser. B 24 (2019) 149–182.
[37] A. Diegel, C. Wang, X. Wang, S. Wise, Convergence analysis and error estimates for a second order accurate finite element method for the Cahn-Hilliard-Navier–Stokes system, Numer. Math. 135 (2013) 495–534.
[38] Y. Liu, W. Chen, C. Wang, S. Wise, Error analysis of a mixed finite element method for a Cahn-Hilliard-Hele-Shaw systemequation, Numer. Math. 135 (2017) 679–709.
[39] W. Chen, Y. Liu, C. Wang, S. Wise, Convergence analysis of a fully discrete finite difference scheme for Cahn-Hilliard-Hele-Shaw equation, Math. Comp. 85 (2016) 2231–2257.
[40] X. Feng, Fully discrete finite element approximations of the Navier–Stokes-Cahn-Hilliard diffuse interface model for two-phase fluid flows, M2AN Math. Model. Numer. Anal. 44 (2006) 1049–1072.
[41] D. Kay, V. Styles, R. Welford, Finite element approximation of a Cahn-Hilliard-Navier–Stokes system, Interfaces Free Bound. 10 (2008) 15–43.
[42] J. Shen, X. Yang, Decoupled energy stable schemes for phase filed models of two phase complex fluids, SIAM J. Sci. Comput. 36 (2014) B122–B145.
[43] J. Shen, X. Yang, H. Yu, Efficient energy stable numerical schemes for a phase field moving contact line model, J. Comput. Phys. 284 (2015) 617–630.
[44] J. van Kan, A second-order accurate pressure-correction scheme for viscous incompressible flow, SIAM J. Sci. Stat. Comput. 7 (3) (1986) 870–891.
[45] J.S. Rowlinson, B. Widom, Molecular Theory of Capillarity, Clarendon Press, Oxford, 1989.
[46] X. Yang, J.J. Feng, C. Liu, J. Shen, Numerical simulations of jet pinching-off and drop formation using an energetic variational phase-field method, J. Comput. Phys. 218 (2006) 417–428.
[47] T. Qin, S. Ragab, P. Yue, Axisymmetric simulation of the interaction of a rising bubble with a rigid surface in viscous flow, Int. J. Multiph. Flow. 52 (2013) 60–70.